Article

Green Fabrication of ZnO Nanoparticles and ZnO/rGO Nanocomposites from Algerian Date Syrup Extract: Synthesis, Characterization, and Augmented Photocatalytic Efficiency in Methylene Blue Degradation

Kamilia Madi [1], Derradji Chebli [1], Hakima Ait Youcef [2], Hichem Tahraoui [1,3], Abdallah Bouguettoucha [1], Mohammed Kebir [4], Jie Zhang [5] and Abdeltif Amrane [6,*]

[1] Laboratoire de Génie des Procédés Chimiques, Department of Process Engineering, University of Ferhat Abbas, Setif 19000, Algeria; madikamilia1998@gmail.com (K.M.); derradji_chebli@yahoo.fr (D.C.); hichemm.tahraouii@gmail.com (H.T.); bouguettoucha@gmail.com (A.B.)
[2] Laboratory of Electrochemistry, Molecular Engineering and Redox Catalysis, Faculty of Technology, Farhat Abbas University, Setif 19137, Algeria; hakimaaityoucef@yahoo.fr
[3] Laboratory of Biomaterials and Transport Phenomena, University of Médéa, Médéa 26000, Algeria
[4] Research Unit in Physical and Chemical Analysis in Fluid and Solid Media (UR-APCMFS/CRAPC), Tipaza 42000, Algeria; medkebir@yahoo.fr
[5] School of Engineering, Merz Court, Newcastle University, Newcastle upon Tyne NE1 7RU, UK; jie.zhang@newcastle.ac.uk
[6] Ecole Nationale Supérieure de Chimie de Rennes, CNRS, ISCR—UMR6226, University Rennes, 35000 Rennes, France
* Correspondence: abdeltif.amrane@univ-rennes1.fr

Abstract: This innovative article provides a detailed description of the successful biosynthesis of zinc nanoparticles (ZnO-NPs) using an aqueous extract of Algerian Date Syrup, also known as molasses. A meticulous process was carried out to determine the optimal calcination temperature for ZnO-NPs, a crucial step in the preparation of these nanoparticles. The study was further extended by creating ZnO/rGOx nanocomposites through a hydrothermal method, varying the concentrations of reduced graphene oxide (rGO) at 5%, 10%, and 15%. The characteristics of the nanocomposites were thoroughly explored, encompassing chemical, optical, and morphological aspects, using sophisticated analysis techniques such as scanning electron microscopy (SEM), UV-visible diffuse reflectance spectroscopy (UV DRS), Fourier-transform infrared spectroscopy (FTIR), and X-ray diffraction (XRD). These analyses provided an in-depth understanding of the structure and properties of the nanocomposites. The centerpiece of this study is the evaluation of the photocatalytic degradation capacity of ZnO-NPs and ZnO/rGOx nanocomposites. These materials have demonstrated their ability to act as cost-effective and environmentally friendly photocatalysts for wastewater treatment. Experiments on methylene blue degradation under UV irradiation were conducted, yielding impressive results: a degradation efficiency of 86.6% was achieved in 140 min using 1 g/L of ZnO-NPs, and this rate reached 100% with the ZnO/rGO catalyst in the same time frame, highlighting its superiority as a photocatalyst. Furthermore, this study examined the variables affecting the photocatalysis experiment, including the solution's pH and the amount of catalyst. The results revealed that the ZnO/rGO photocatalyst reached its optimal efficiency under neutral pH conditions and at a concentration of 1 g/L, providing crucial information for practical use of these materials. This enriched article highlights the promising potential of ZnO-NPs and ZnO/rGOx nanocomposites as efficient photocatalysts for methylene blue degradation, paving the way for significant environmental applications in wastewater treatment.

Keywords: zinc oxide; reduced graphene oxide; green synthesis; photocatalysis; methylene blue

1. Introduction

The field of photocatalysis research and development has seen substantial growth in recent years, as illustrated by the increasing number of publications on this subject matter, mainly due to its potential applications in environmental technologies such as hydrogen production [1], organic synthesis, medicinal chemistry, and water treatment [2].

The emergence of nanotechnology could have a major impact on the field of photocatalysis for the production of new materials, typically semiconductors. One of the biggest advantages of nanostructures is their ability to exhibit exceptional properties, which can be used to create new photocatalysts or improve existing ones [3]. Furthermore, nanotechnologies enable the development of more efficient and energy-saving photocatalytic systems to address current environmental and energy challenges [4].

It is undoubted that the advancements in nanomaterials synthesis techniques are resulting in the emergence of new materials with desired chemical and physical properties [5]. Nanoparticles can be synthesized using different techniques, which are generally classified into two primary methods. The first approach, known as the bottom-up technique, employs chemical processes such as hydrothermal, co-precipitation, electrochemical, pyrolysis, sonochemical, photochemical, microemulsion, microwave, redox, and sol–gel processes. These methods involve the combination of individual atoms or molecules to produce nanoparticles [6]. The second method is characterized by a top-down approach, which requires the use of physical techniques, such as laser ablation, inert gas condensation, sonication, electric arc discharge, lithography, and the radiofrequency (RF) plasma method. These physical techniques consume a lot of energy and raise the temperature of the surrounding air around the source material since it takes so long for them to achieve thermal stability. Additionally, these methods occupy a large amount of space, especially in the case of furnaces [7]. The chemical processes have undesirable effects on the environment and are environmentally unfriendly [8] due to the use of harsh reducing agents such as sodium citrate, sodium borohydride, and organic solvents.

Generally, the concept of "Green Synthesis" refers to the application of ecological principles of "green chemistry", such as plant extracts and microorganisms such as fungal, bacteria, and algae, to the biosynthesis of nanoparticle oxides, allowing pure and safe nanoparticles to be obtained from different organisms such as fungi, plants, bacteria, and actinomycetes [9]. "Green synthesis" using biomaterials comprises a diverse array of compounds, including proteins, flavonoids and polyphenols, which have the potential to substitute hazardous chemical products as reducing agents, in order to lower the valence state of metal ions. Consequently, it offers many benefits, including biocompatibility, low toxicity, simplified production, improved profitability, and the possibility of regulating the synthesis process [10].

Metallic nanoparticles can be fabricated using extracts from various biological sources, both cellular and cell-free, as illustrated in Figure 1. It is essential to ensure that the nanoparticle synthesis process aligns with the principles of green chemistry [11]. This involves meticulous consideration of factors such as the choice of environmentally friendly solvents, the use of eco-friendly reducing agents, and the selection of non-toxic materials for nanoparticle stabilization. Furthermore, it has been established that compounds like peptides, polyphenolics, sugars, vitamins, and aqueous components derived from plant extracts demonstrate compatibility and efficacy in the synthesis of nanoparticles [12].

Date Syrup, also known as date molasses or date honey, is a thick, sweet syrup made from boiled and reduced dates. This substance is a natural source rich in sugars, vitamins, antioxidants, and minerals [13]. Recently, interest in the use of natural products such as date molasses in the "green synthesis" of nanoparticles and other materials has increased significantly. Date molasses contains natural reducing agents, such as sugars (fructose and glucose), alkaloids, terpenoids, and polyphenols, which seem to be a prominent solution to easily reduce metal ions and form nanoparticle catalysts [14].
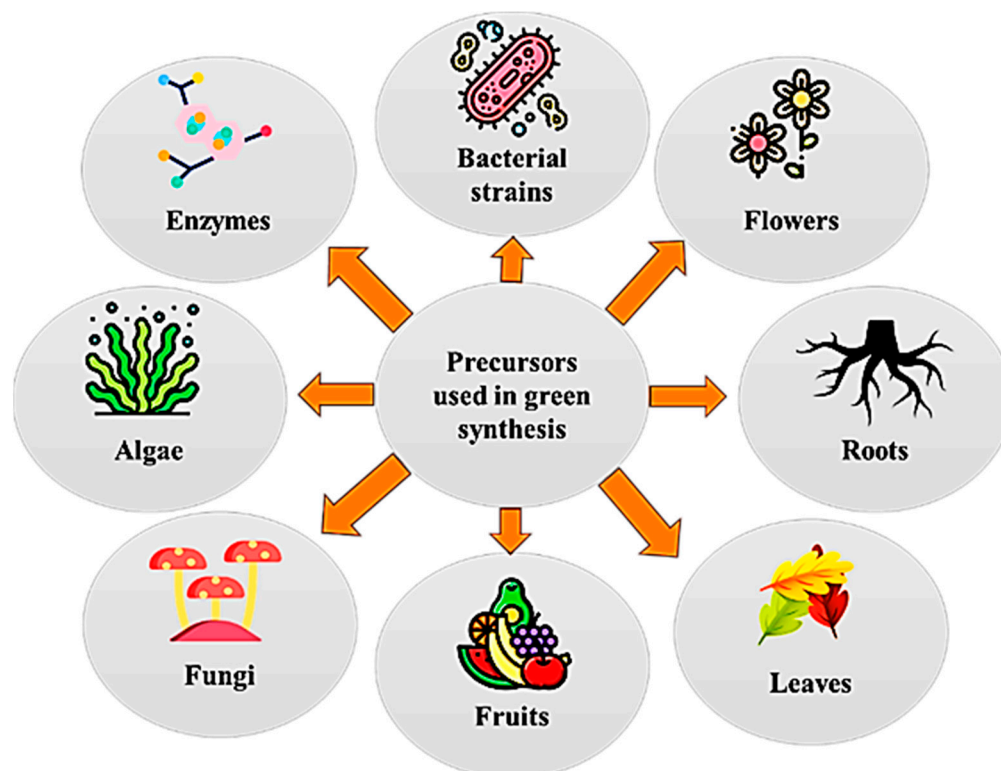
Figure 1. The precursors used for green synthesis.

In particular, ZnO nanoparticles have become a very interesting topic due to their ease of preparation, low production cost, and safety [15]. Due to its high catalytic activity, ZnO is a significant semiconductor photocatalyst. It can effectively destroy organic material when exposed to ultraviolet radiation, making it useful in a variety of environmental applications like the treatment of wastewater and air purification [15].

In previous studies, graphene oxide (GO), reduced graphene oxide (rGO), and their derivatives have found extensive applications in wastewater treatment for the removal and degradation of organic pollutants [16].

This widespread use in many fields is attributed to their exceptional adsorption, oxidation, and catalytic properties, as well as their large pore volume, huge specific surface area, high electrical conductivity, diverse surface chemical composition, and impressive length-to-diameter ratio [17]. It has been reported that the combination of materials boosts photocatalytic activity; in this context, to elaborate, graphene serves a thermodynamic role in crafting heterojunction photocatalysts capable of responding to a wide spectrum of light or in the doping of semiconductors possessing wide bandgaps [18].

Additionally, graphene's kinetic utilization enhances photocatalytic efficiency by capitalizing on its remarkable adsorption capacity for both organic and inorganic contaminants [19]. Given these factors, the integration of graphene with diverse semiconductors has emerged as a promising avenue for advancing research in this field [18].

In this study, ZnO/rGOx nanocomposites were manufactured and subjected to comprehensive characterization using various techniques, including X-ray diffraction (XRD), Fourier-transform infrared spectroscopy (FTIR), and scanning electron microscopy (SEM). Additionally, the analysis of the optical properties of these nanocomposites was conducted using UV-visible spectrophotometry to assess their UV absorption capacity and determine the width of the band gap. Concurrently, this study examined the impact of parameters such as calcination temperature, catalyst dosage, and solution pH on the degradation efficiency of the compounds. Cycling tests were performed to confirm the stability of the ZnO/rGOx nanocomposite, and a degradation mechanism was proposed, based on the generation of electron–hole pairs and the attacking of the dye by hydroxyl and superoxide

radicals. This research highlights the remarkable potential of ZnO/rGOx nanocomposites in water treatment for the removal of organic pollutants. However, it is essential to note that future research efforts will be needed to adapt these nanocomposites for practical wastewater treatment applications.

This study significantly enriches our understanding of advanced photocatalytic materials and their potential applications in environmental remediation. A primary contribution lies in the innovative use of ZnO/rGOx nanocomposites, a unique combination of ZnO and rGOx, which introduces a fresh perspective on enhancing photocatalytic performance, particularly in the degradation of methylene blue. The research achieves a notable level of depth and sophistication through its comprehensive materials characterization, encompassing crystallographic verification via XRD, the identification of functional groups using FTIR, and the detailed examination of material morphology through SEM. The most remarkable breakthrough, however, is the compelling evidence of a substantial enhancement in the photocatalytic efficiency of ZnO/rGOx nanocomposites in comparison to pure ZnO. This carries profound implications for water treatment, as it addresses the challenge of organic pollutant removal with unprecedented effectiveness. Moreover, this study goes beyond material synthesis and characterization by systematically exploring the influence of various reaction parameters and underlining the stability of these nanocomposites, reinforcing their potential for practical and sustainable applications in real-world wastewater treatment scenarios. In sum, this research represents a significant enrichment of our knowledge in the field, setting the stage for promising advancements in the quest for improved water quality and the mitigation of environmental pollution.

2. Results

2.1. Characterization

2.1.1. X-ray Diffraction

In Figure 2, the XRD patterns of both pure ZnO and the ZnO/rGO nanohybrid photocatalysts are presented. The observed diffraction peaks in the XRD pattern of the synthesized photocatalysts closely match the characteristic pattern of the hexagonal wurtzite phase of ZnO, as indicated by its reference in the Joint Committee on Powder Diffraction Standards JCPDS database under No. 36-1451 [20]. Specifically, the XRD pattern displays distinct peaks at various 2θ angles, namely 31.6°, 34.28°, 36.11°, 47.4°, 56.5°, 62.5°, 67.8°, 68.9°, and 76.8°. These peaks correspond to the 100, 002, 101, 102, 110, 103, 112, 201, and 004 crystalline planes of ZnO [21]. The presence of distinct diffraction peaks at 26.2° (002) for rGO strongly indicates the effective anchoring of ZnO nanoparticles onto the rGO [22]. This alignment of observed peaks with the standard wurtzite phase of ZnO confirms the crystalline structure of the synthesized photocatalysts and suggests the successful formation of ZnO/rGO nanohybrids. The crystallite sizes shown in Table 1 were calculated using the Scherrer formula

$$D = \frac{K\lambda}{\beta \, COS(\theta)} \tag{1}$$

where:

- D represents the average crystallite size.
- K is the Scherrer constant, which is approximately 0.9 and depends on the crystallite shape.
- λ is the wavelength of the X-ray radiation used for the diffraction.
- β is the full width at half-maximum (FWHM) of the XRD peak, measured in radians.
- θ is the Bragg angle, which is half of the angle between the incident X-ray beam and the scattered X-ray beam.
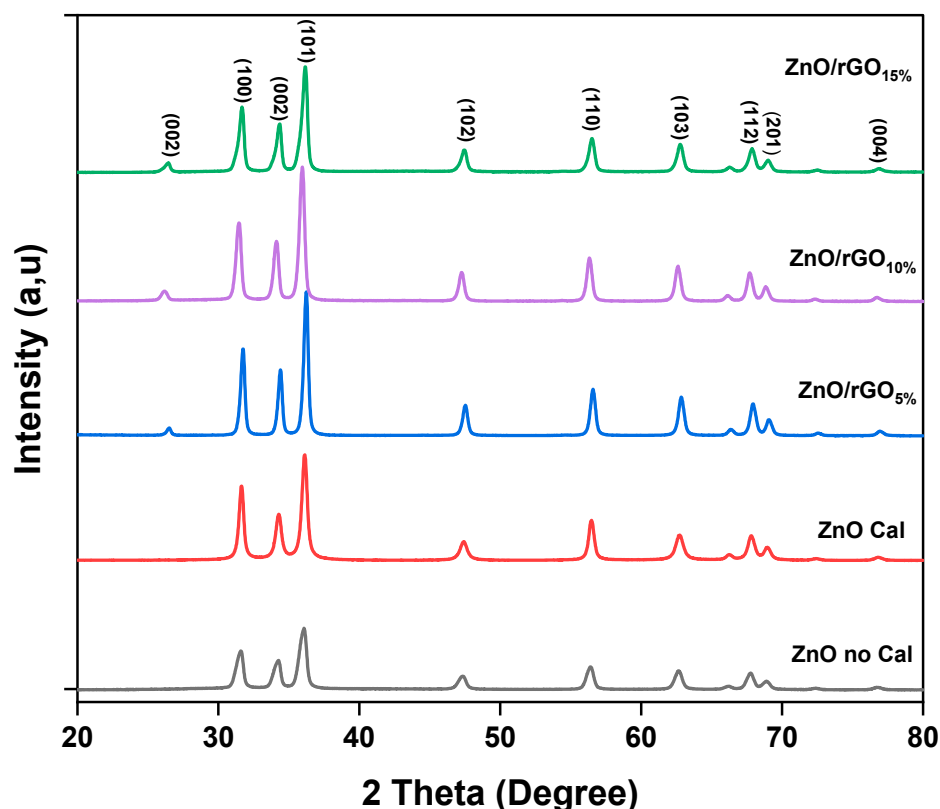
Figure 2. XRD patterns of pure ZnO and ZnO-rGO$_x$.

Table 1. The crystallite size of the different samples.

Samples	Crystallite Size (nm)
ZnO non-calcined	13.99
ZnO calcined at 550 °C	14.18
ZnO/rGO 5%	21.42
ZnO/rGO 10%	20.06
ZnO/rGO 15%	17.31

ZnO/rGO nanohybrids were observed to have bigger crystallite sizes when compared to pure ZnO. When ZnO is combined with rGO, the interactions between ZnO nanoparticles and rGO lead to a restructuring of ZnO particles. This particular process promotes the growth of pre-existing crystallites, leading to a subsequent increase in their size dimension. This result shows that larger crystal sizes can be associated with improved photocatalytic activity or enhanced performance in specific applications. However, it is essential to understand the underlying mechanisms to design and optimize nanomaterials according to the specific requirements of each application [23].

2.1.2. Fourier-Transform Infrared Spectroscopy

The absorption bands in the FTIR spectrum of the ZnO-rGO composite presented in Figure 3 reveal crucial insights. The absorption band in the range of 3600–3200 cm^{-1} corresponds to the stretching vibrations of (OH) groups, either from water or hydroxyl groups linked to the composite's surface from moisture, polyphenols, and some N-H of amine overlapping [24], bearing significance for surface chemistry [25]. The band at 2340 cm^{-1} is associated with the absorption of atmospheric carbon dioxide (CO_2), originating from the natural CO_2 content in the air during the analysis, contributing to specific spectral features [26] or aldehyde peak due to C=O stretching vibration [27]. The 1700–1600 cm^{-1} region is associated with the angular deformation vibration (OH)

groups of adsorbed water groups [28], while the range of 1600–1500 cm^{-1} is linked to vibrations of carbonyl groups or other bands, (C=C), (−CO), and (C=O), from the organic residue of the extract (the phenolic and flavonoids) absorbed on the surface of ZnO [29]. The 1500–1400 cm^{-1} region may be attributed to vibrations involving hydroxyl groups (O–H) or carboxylate of zinc groups [30]. Lastly, the band around 500–400 cm^{-1} is the fingerprint region which represents the bending and deformation vibrations of Zn–O of the crystalline lattice of nanoparticle metal oxide ZnO [31], consistent with previous findings in the literature [32]. The decrease in infrared peak intensity upon adding reduced graphene oxide (rGO) to zinc oxide (ZnO) can be attributed to various factors associated with composite formation. rGO's strong adsorption capacity may lead to the adsorption of ZnO particles onto rGO sheets, reducing ZnO availability for infrared signals. Interactions between rGO and ZnO induce changes in crystal structure, affecting vibrational modes and peak characteristics. The incorporation of rGO into the ZnO matrix forms a composite with unique properties, influencing infrared peak intensities. Additionally, rGO's conductive nature affects electronic properties, altering ZnO's interaction with infrared radiation and contributing to changes in peak intensity. Moreover, the difficulty in distinguishing between ZnO and ZnO/rGO may be due to the reduction of graphene during the preparation of the process.
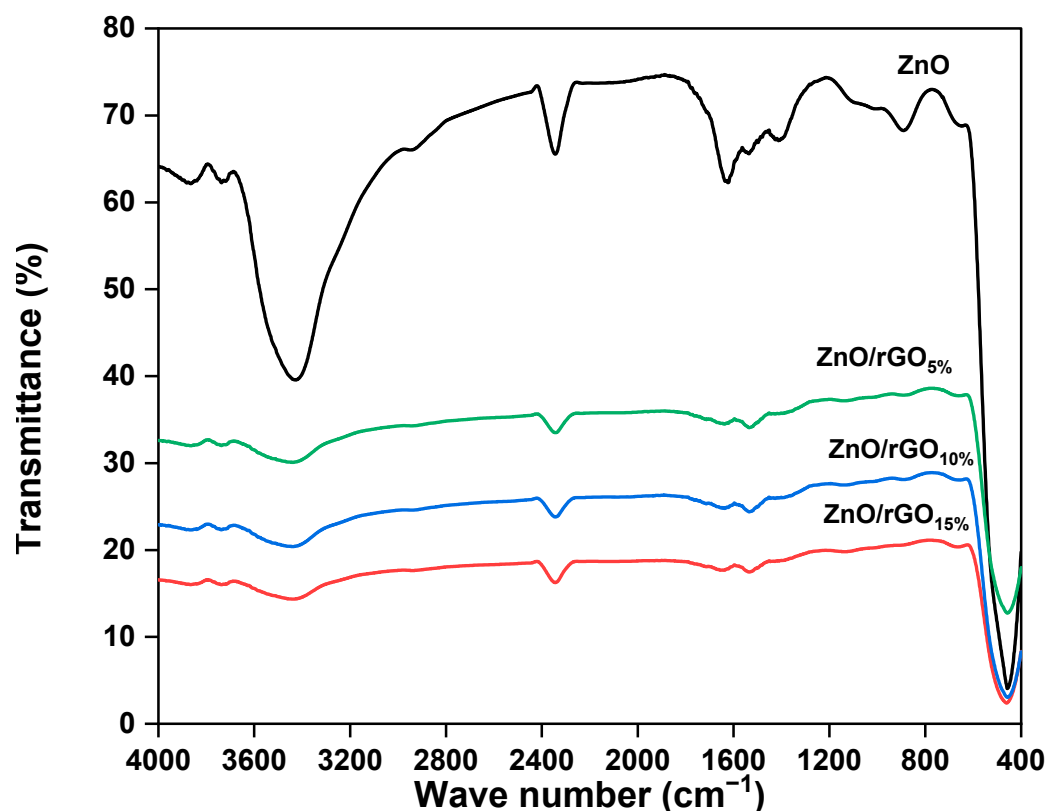
Figure 3. FT-IR spectra of ZnO and ZnO/rGO$_x$ nanocomposite.

2.1.3. Scanning Electron Microscopy Images

The morphology of ZnO/rGO was assessed using scanning electron microscopy (SEM). In Figure 4a, it is evident that the ZnO nanoparticles exhibit diverse shapes. This phenomenon can be attributed to the interaction with organic components from the molasses extract. Additionally, Figure 4b clearly shows that the ZnO nanocrystals are evenly spread out on the graphene sheets (marked with a red circle). This confirms the formation of the ZnO/rGOx heterojunction [33].

Figure 4. SEM images of (**a**) pure ZnO; (**b**) ZnO/rGO$_{10\%}$.

2.1.4. UV-Visible Diffuse Reflectance Spectroscopy

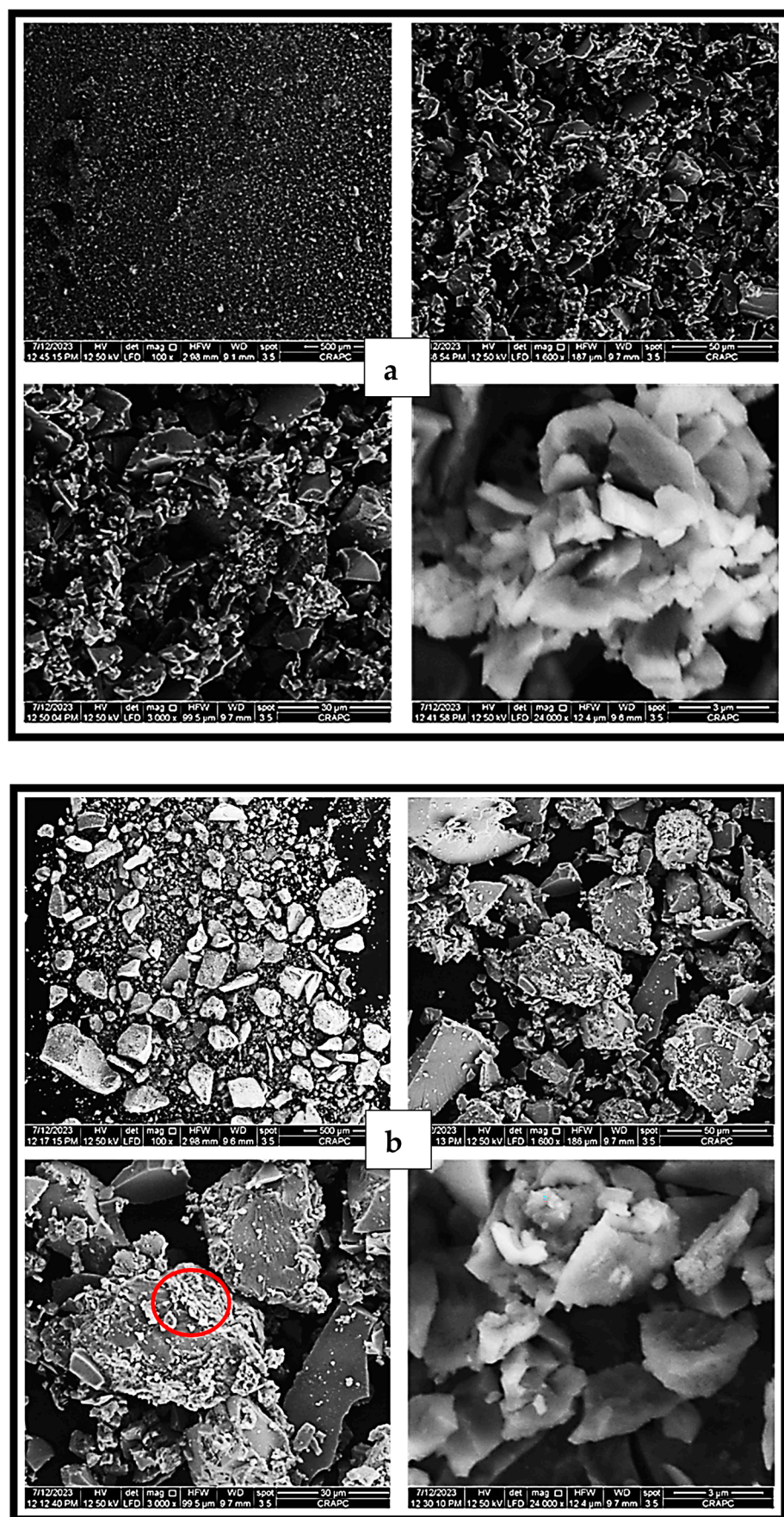The optical characteristics of the ZnO and ZnO/rGO samples were assessed via UV-visible diffuse reflectance spectroscopy (DRS). As depicted in Figure 5, the DRS spectra of the ZnO samples demonstrated pronounced light absorption in the ultraviolet region [34]. This absorption phenomenon originates from electron transitions occurring between the valence and conduction bands of ZnO when subjected to UV light irradiation. Notably, a distinct absorption peak, observed at approximately 364 nm, was evident across all examined samples. The optical band gap 'E$_g$' is calculated by Tauc's plot.

$$(\alpha h\nu)^{1/2} = A(h\nu - E_g) \tag{2}$$

where:

- α is the absorption coefficient.
- $h\nu$ is the photon energy.
- A is a constant.
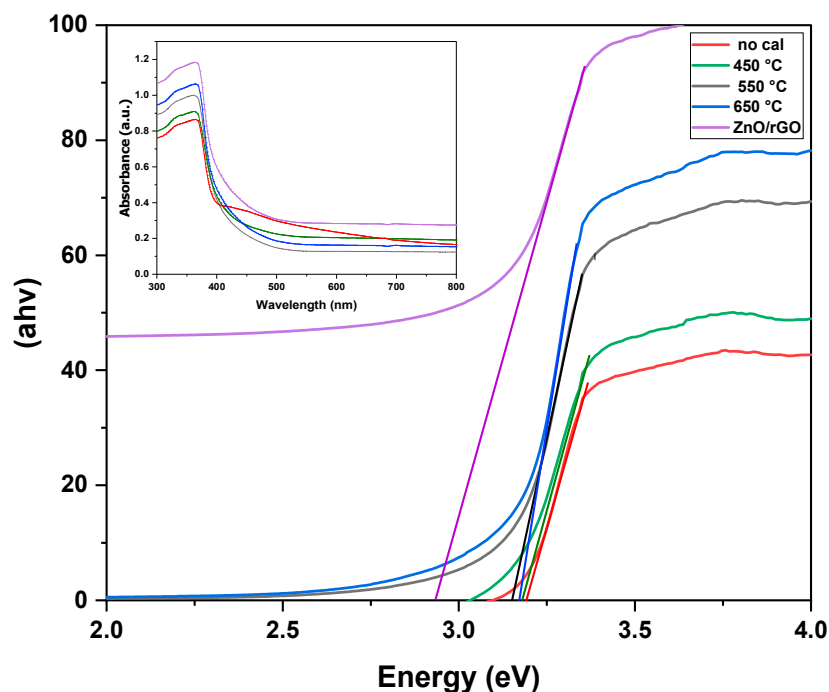- E$_g$ is the bandgap energy.

Figure 5. Band gap energies and UV-vis diffuse reflectance spectra of ZnO at different calcination temperatures and ZnO/rGO$_{10\%}$.

The initial band gap value for as-synthesized ZnO nanoparticles is 3.19 eV. However, after undergoing calcination at different temperatures (450 °C, 550 °C, and 600 °C), the band gap decreases to 3.18 eV, 3.17 eV, and 3.15 eV, respectively. This decrease is linked to changes in the crystallite size of the nanoparticles, which tends to increase with higher calcination temperatures. Essentially, as the calcination temperature rises, the nanoparticles grow larger, leading to a smaller band gap [35].

When rGO is added to ZnO, the value of ZnO's bandgap energy decreases from 3.15 to 2.93 eV and this reduction is due to several factors. rGO acts as a dopant, introducing additional charges into the material's structure, which shifts energy levels and reduces the bandgap energy [36]. Additionally, as a good conductor of electricity, rGO can interact with ZnO, causing a redistribution of electronic energy levels and potentially altering the crystalline structure of the composite material [37]. This reduction in the bandgap energy makes the composite material more conductive, which can be advantageous in various applications.

2.2. *Photocatalytic Results*

2.2.1. Effect of Calcination Temperature on the Photocatalytic Activity of ZnO NPs

To investigate the effect of calcination temperature on the photocatalytic activity of the ZnO semiconductor, a series of ZnO samples were prepared by the green method at different calcination temperatures. The photocatalytic activity was examined by the photodegradation of MB. The photocatalytic performance of calcined ZnO (98% for ZnO calcined at 550 °C) significantly increased compared to that of non-calcined ZnO (73.6%). The activity of the ZnO NPs increased when the calcination temperature increased from 450 to 550 °C but slightly decreased when the calcination temperature increased to 600 °C. Further, the rate constant "k" value for ZnO calcined at 550 °C was 0.01565 min^{-1} against 0.00393 min^{-1} for non-calcined ZnO, indicating higher photocatalytic activity for the catalyst calcined at 550 °C (Figure 6). The "k" values are shown in Table 2. The influence of calcination temperature on the photocatalytic activity of ZnO is related to the morphological, optical, and surface properties of the ZnO NPs [38,39].
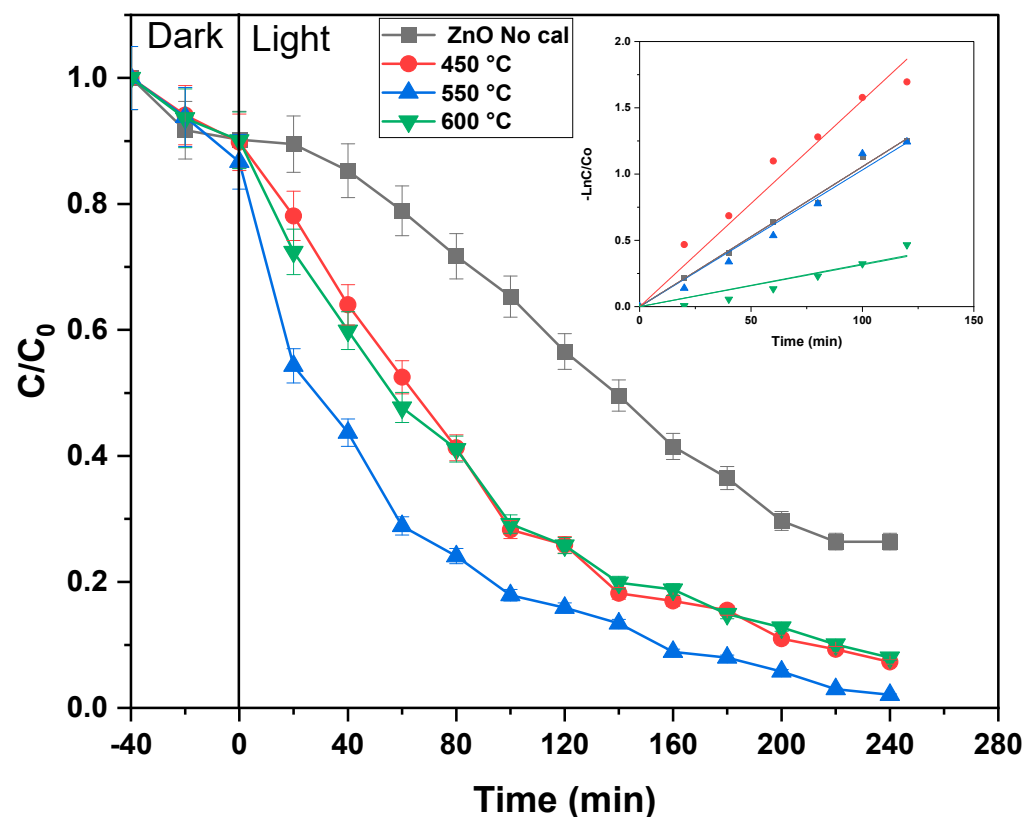
Figure 6. Effect of calcination temperature on the photocatalytic activity of ZnO for the photocatalytic degradation of MB (neutral pH, catalyst 1 g/L, [MB] = 10 mg/L).

Table 2. The rate constant 'k' of MB degradation with ZnO calcined at different temperatures.

Samples	Non-Calcined	600 °C	550 °C	450 °C
K (min^{-1})	0.0039	0.0106	0.0156	0.0103
R^2	0.94113	0.99285	0.99026	0.99124

2.2.2. Photocatalytic Activity of ZnO/rGO$_x$

The photocatalytic effectiveness of both ZnO (calcined at 550 °C) and ZnO/rGO nanohybrid photocatalysts was assessed through the degradation of MB under UV light irradiation, as illustrated in Figure 7. In comparison, pure ZnO achieved a degradation of only 85.4% for MB after 140 min of irradiation. In contrast, the ZnO/rGO nanohybrids

exhibited significantly enhanced photocatalytic performance, with degradation efficiencies of 96%, 100%, and 88.6% for ZnO/rGO_5, ZnO/rGO_{10}, and ZnO/rGO_{15}, respectively, after 140 min of irradiation. Therefore, the incorporation of rGO resulted in a notable reduction in the time required for the complete degradation of MB, decreasing it from 240 min to 140 min. Table 3 shows that the reaction rate constant "k" exhibits an ascending trend with values of 0.0156, 0.0106, 0.0272, and 0.0103 for ZnO, $ZnO/rGO_{5\%}$, $ZnO/rGO_{10\%}$, and $ZnO/rGO_{15\%}$, respectively.
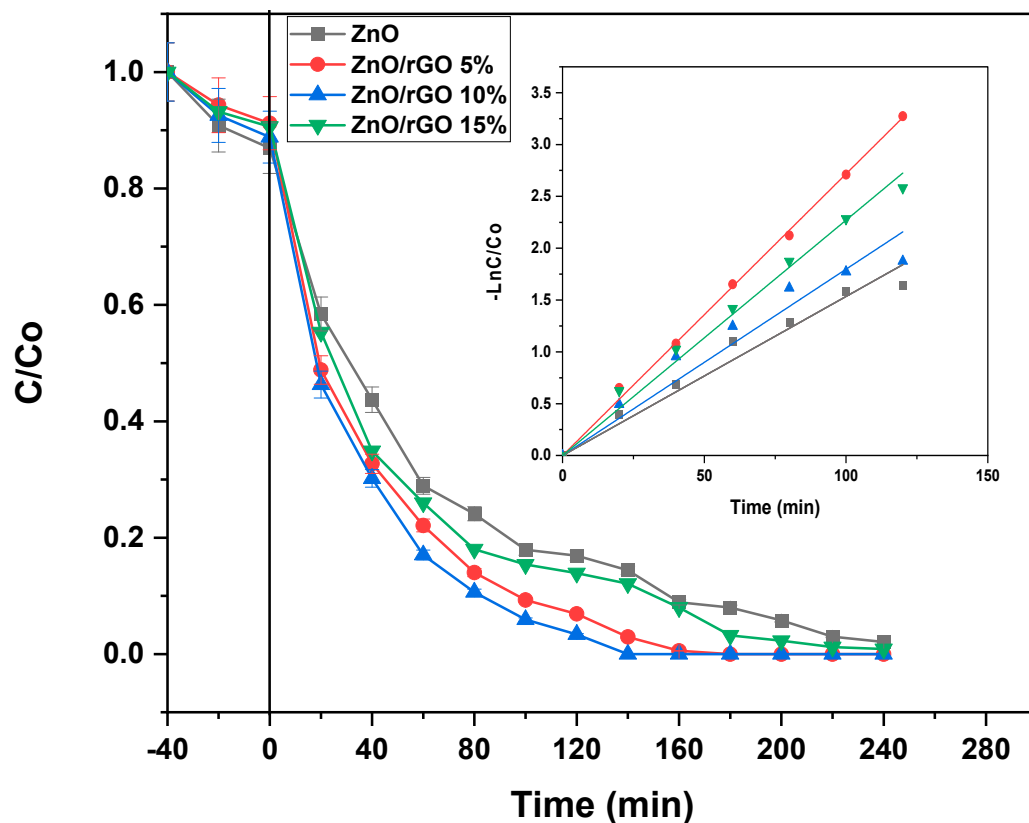

Figure 7. Photodegradation of MB dye by ZnO/rGO_x (x = 5, 10 and 15%) (neutral pH, catalyst 1 g/L, [MB] = 10 mg/L).

Table 3. The rate constant 'k' of MB with ZnO/rGO_x.

Samples	ZnO	$ZnO/rGO_{5\%}$	$ZnO/rGO_{10\%}$	$ZnO/rGO_{15\%}$
K (min^{-1})	0.0156	0.0106	0.0272	0.0103
R^2	0.99026	0.99628	0.99944	0.98212

The deliberate selection of ZnO calcined at 550 °C as the reference for the entire study, including compounds coupled with rGO, was based on preliminary photodegradation tests at varying calcination temperatures. Notably, the optimal result of 86.6% degradation was consistently achieved at 550 °C (ZnO calcined at 550 °C without coupling with rGO).

It is crucial to note that rGO acts as an electron trapper, thereby preventing their recombination within the semiconductor material. This characteristic of rGO is pivotal as it promotes a faster and more efficient degradation of the dye. By averting electron recombination, rGO enables the excited electrons to interact with the dye, thus facilitating chemical degradation reactions [40]. Furthermore, rGO possesses a large specific surface area and a two-dimensional sheet-like structure, allowing for increased adsorption of organic pollutants on its surface. This creates more active sites for photocatalytic reactions to occur [41].

2.2.3. Effect of Catalyst Dosage

The quantity of catalyst is a crucial factor in the production of active radicals in photocatalytic degradation reactions. However, an excessive amount of catalyst can impede the penetration of incident light, and hence potentially reducing the degradation process. Therefore, the influence of catalyst dosage on the degradation of MB ([MB] = 10 mg/L) was systematically investigated by varying the quantity of ZnO/rGO nanocomposite within the range from 0.25 g/L to 2 g/L, while maintaining neutral pH conditions and subjecting the reaction to 140 min of irradiation. As the catalyst dosage was incrementally increased from 0.25 to 1 g/L, the degradation efficiency experienced a corresponding rise, progressing from 62.3% to reach a complete degradation of 100%. However, when the catalyst dosage was further elevated to 2 g/L, the degradation efficiency exhibited a decrease to 67.4% (Figure 8). This observed enhancement in degradation with the initial increase in catalyst dosage, from 0.25 to 1 g/L, can be attributed to the greater available catalyst surface area. This increased surface area facilitated the enhanced absorption of photons, thus promoting the photocatalytic process through the greater number of (e^-, h^+) pairs, resulting in the generation of more active radicals [42]. The reduction in the degradation rate beyond a catalyst dosage of 1 g/L can be attributed to the increasing solution turbidity and the adverse effects associated with surpassing the optimal photocatalyst dose. This finding is supported by the first-order rate constants shown in Table 4 for various masses of the catalyst, which gave trend values of 0.0156, 0.0106, 0.0272, and 0.0103 for ZnO, ZnO/rGO$_{5\%}$, ZnO/rGO$_{10\%}$, and ZnO/rGO$_{15\%}$, respectively.
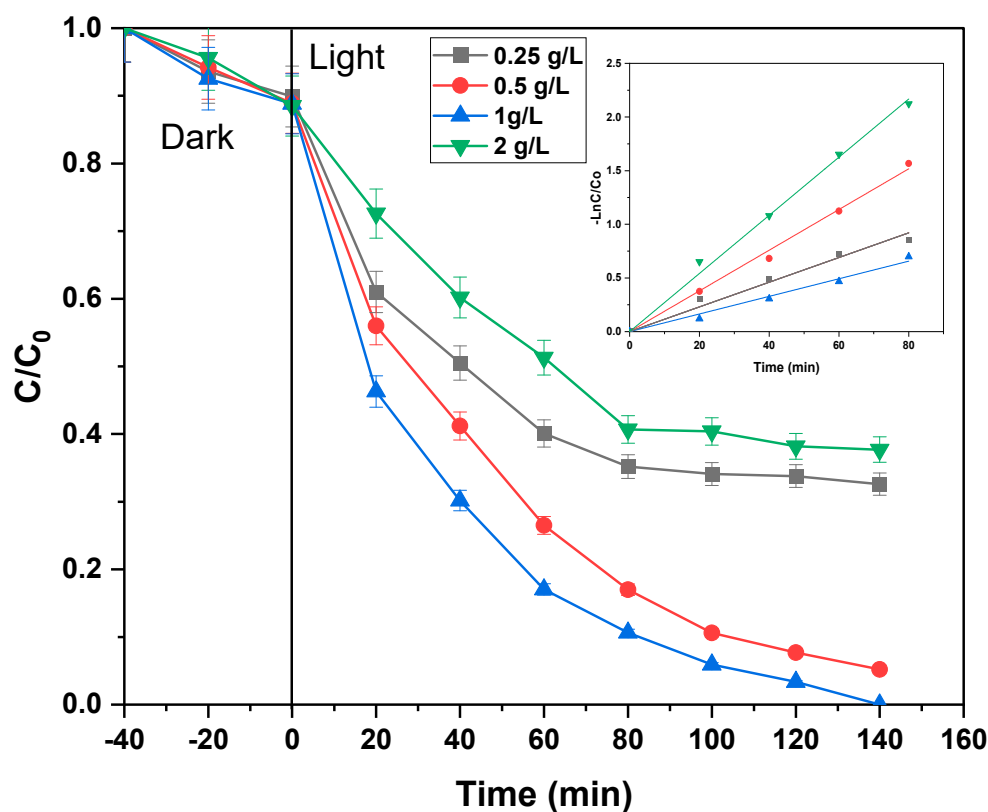

Figure 8. Effect of catalyst dose on photodegradation of MB by ZnO/rGO$_{10\%}$ (neutral pH, [MB] = 10 mg/L).

Table 4. Rate constant K of degradation of MB with different dosages of ZnO/rGO.

Dosage (g/L)	0.25	0.5	1	2
K (min^{-1})	0.0115	0.0188	0.0272	0.0082
R^2	0.99219	0.99801	0.99944	0.99401

These effects encompass particle agglomeration, diminished UV light penetration, restricted mobility of reactants, increased recombination of electron–hole pairs, saturation of active surface sites, and the emergence of undesired side reactions. Consequently, precise control of photocatalyst dosage is imperative to mitigate these issues and fine-tune the photocatalytic process for applications [43].

Regarding the evolution of K values, a notable observation was the increase in the kinetic constant only for doses from 0.25 to 1 g/L, followed by a decrease at the 2 g/L dose. The correlation between methylene blue degradation and the kinetic constant derived from linear regression takes on particular significance. It sheds light on the relationship between the efficiency of the degradation process and the speed of that degradation. The kinetic constant, representing the reaction rate in the degradation process, holds central importance. A higher kinetic constant is indicative of a rapid reaction, signaling increased efficiency in methylene blue degradation. Conversely, a lower kinetic constant may suggest a slower reaction, potentially linked to a decrease in efficiency in the degradation process. This nuanced interpretation underscores the crucial importance of the kinetic constant in a comprehensive understanding of the kinetics of methylene blue degradation.

Examining the K values for each dose from Table 4 (0.25 g/L, 0.5 g/L, 1 g/L, 2 g/L) revealed a significant variation. K values increased from 0.0115 to 0.0272 for doses from 0.25 to 1 g/L, suggesting a positive correlation between the substance concentration and the degradation rate. However, the K value then decreased to 0.0082 for the 2 g/L dose. This fluctuation highlights the specific influence of concentration on the degradation kinetics, reinforcing the importance of the kinetic constant in evaluating the efficiency of the methylene blue degradation process.

2.2.4. Effect of Reaction pH

In previous studies, researchers have highlighted the significant effect of the initial pH value in the reaction mixture, emphasizing its substantial influence on the photocatalytic performance [44]. The impact of solution pH on the photocatalytic degradation of MB was investigated at initial pH levels of 4, neutral (approximately 7), 8, and 10. Figure 9 shows that the decomposition rate of MB with ZnO/rGO10% catalysis is significantly influenced by the pH of the dye solution, with the catalyst exhibiting greater efficiency in a neutral environment. With a degradation rate of 100% at neutral pH, this value decreases to 75% at pH 4. Subsequently, an increase in the rates is observed, with 90% and 94% corresponding to pH 9 and 10, respectively. The photocatalytic activity of $ZnO/rGO_{10\%}$ is typically higher under neutral to slightly basic pH values for several reasons. For the most precise assessment, the kinetic degradation constant for MB has been computed at various pH values, and these values are delineated in Table 5. First, $ZnO/rGO_{10\%}$ exhibits greater stability at neutral pH levels, as extremes in acidity or alkalinity can lead to rapid dissolution or corrosion, shortening the material's lifespan [45]. Second, at neutral pH, the recombination of charge carriers (electrons and holes) is generally reduced, allowing photoexcited electrons a better chance to react with other reactive species before recombining, thus enhancing photocatalytic efficiency [11]. Third, the balance between surface protonation and deprotonation at neutral pH creates a surface conducive to photocatalytic reactions by enabling the formation of hydroxyl radicals (●OH) and the generation of electron–hole pairs (e^-/h^+) [46]. Lastly, neutral pH conditions are well suited for degrading a wide range of organic pollutants, making them the preferred choice for photocatalytic applications due to the equilibrium they strike between material stability and effectiveness in degrading diverse pollutants.
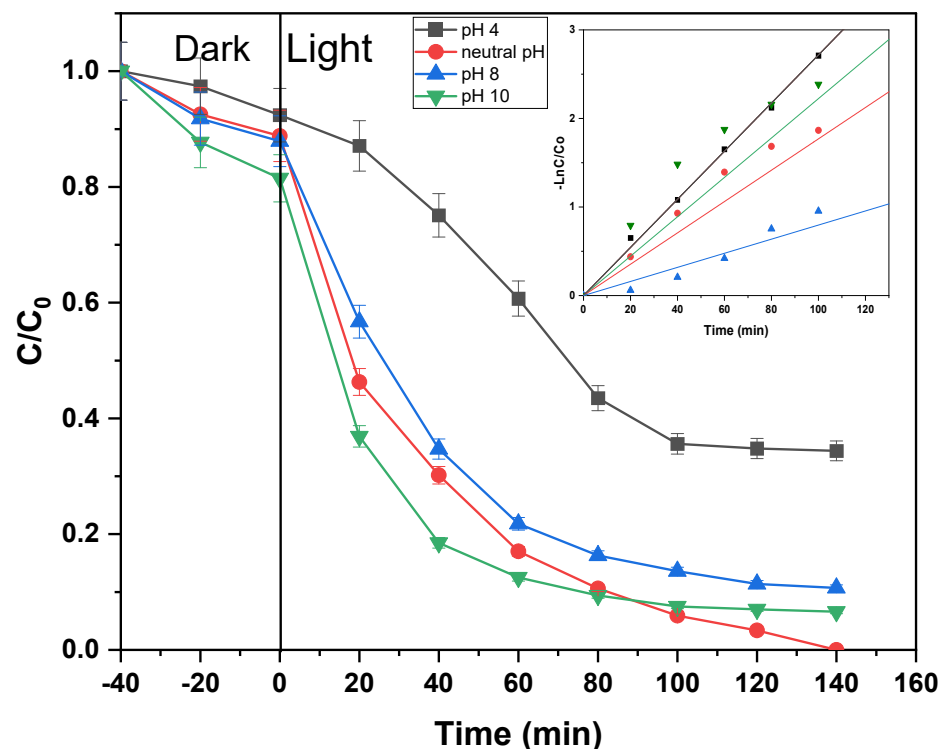
Figure 9. Effect of reaction pH on photodegradation of MB by ZnO/rGO$_{10\%}$ (catalyst 1 g/L, [MB] = 10 mg/L).

Table 5. Rate constant K of degradation of MB with ZnO/rGO at different pHs.

pH	4	Neutral	8	10
K (min^{-1})	0.0079	0.0278	0.0177	0.0223
R^2	0.97781	0.99944	0.97807	0.9538

Regarding the evolution of K values (Table 5), the K values for MB degradation exhibited notable variations at different pH levels. At pH 4, the observed K value of 0.0079 min^{-1} indicates a relatively slow degradation rate, pointing to reduced efficiency under acidic conditions. This could be attributed to the inhibitory effect of excess protons on the degradation process.

Conversely, at neutral pH, the substantial increase in the K value to 0.0278 min^{-1} signifies a significantly faster reaction rate. This suggests that neutral pH is optimal for methylene blue degradation, reflecting higher efficiency compared to acidic conditions.

Moving to pH 8, the K value of 0.0177 min^{-1}, while lower than at neutral pH, still indicates a reasonably efficient degradation process under slightly alkaline conditions. The moderate reaction rate at pH 8 suggests effective degradation, though not as rapid as observed at neutral pH.

At pH 10, the K value of 0.0223 min^{-1} falls between the rates observed at neutral pH and pH 8. This indicates a moderate reaction rate and efficiency in the degradation process under more alkaline conditions. Degradation at pH 10 occurs faster than under acidic conditions but not as rapidly as at neutral pH.

The nuanced variations in K values across different pH levels underscore the sensitivity of methylene blue degradation kinetics to changes in acidity and alkalinity. The optimal efficiency observed at neutral pH highlights the importance of considering environmental conditions in understanding and optimizing the degradation process.

2.3. Cycling Test of the Photocatalytic Degradation of Methylene Blue under UV Light

Photostability stands as a pivotal factor in determining the practical viability of a photocatalyst. In a bid to comprehensively evaluate the structural integrity and catalytic endurance of the $ZnO/rGO_{10\%}$ nanocomposite, a sequence of five successive tests centered around the photocatalytic degradation of MB was meticulously executed. The recycling protocol post UV-light-assisted MB degradation encompasses several crucial steps.

Initiating the process, the composite was meticulously recovered through a precision-centric centrifugation process following each photocatalytic test. Subsequently, a thorough four-cycle washing procedure was set in motion, employing a thoughtfully concocted mixture of distilled water and ethanol, culminating in the final cycle using double-distilled water. The material underwent a five-hour UV light treatment in double-distilled water, ensuring the comprehensive elimination of any lingering MB residues post-photocatalytic decomposition.

Post-UV treatment, the ZnO/rGO material was delicately recovered and subjected to a drying regimen at 60 °C for 24 h, a crucial step ensuring its preservation for subsequent cycles. This meticulous and comprehensive approach serves as a robust framework for assessing the longevity and reusability of the ZnO/rGO composite within the realm of photocatalytic applications.

Figure 10 visually encapsulates the outcomes of five consecutive cycles of MB photodecomposition, revealing a steadfast maintenance of photocatalytic efficiency. This noteworthy finding underscores the inherent stability of the ZnO/rGO nanocomposite, emphasizing its resilience and reliability over successive photocatalytic test cycles.
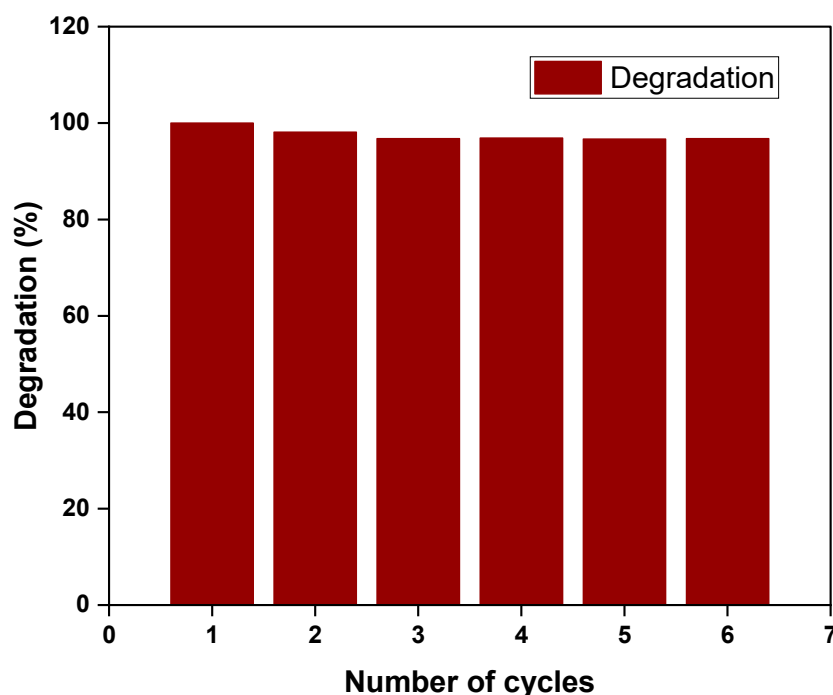

Figure 10. Comparative performance of reused ZnO/rGO photocatalyst.

2.4. Effect of Scavengers

The investigation aimed at identifying the primary species responsible for the degradation of MB in the presence of simple ZnO (calcined at 550 °C) and $ZnO/rGO_{10\%}$ catalysts was carried out following the scientific method. The experimental conditions encompassed a neutral pH environment, with a catalyst dose of 1 g/L and a methylene blue (MB) concentration of 10 mg/L. Active trapping agents, known as scavengers, were employed in this study. Specifically, ethanol was used for hydroxyl radicals $^{\bullet}OH$, $K_2Cr_2O_7$ for electrons e^- [47], and (Na_2-EDTA) for holes h^+ [44]. The experiments were meticulously conducted

under predefined optimal conditions, with a ZnO irradiation duration of 240 min and a ZnO/rGO irradiation duration of 140 min. The resulting impact of these scavengers on the photodegradation of MB using ZnO and ZnO/rGO catalysts is visually presented in Figure 11.
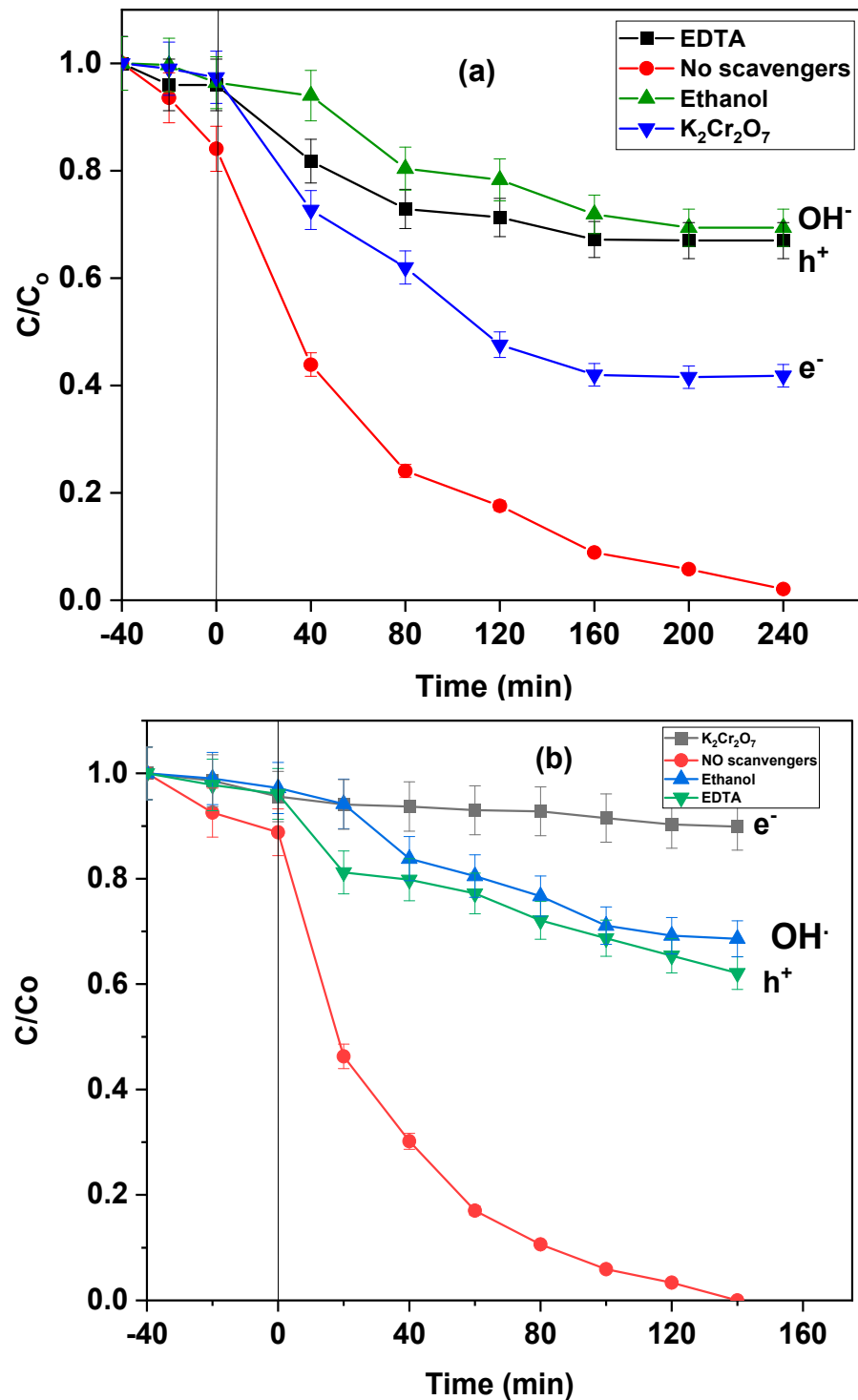

Figure 11. Effect of scavengers on the photocatalytic activity of ZnO (**a**) and ZnO/rGO (**b**) (neutral pH, catalyst 1 g/L, [MB] = 10 mg/L).

Using ethanol as a scavenger to sequester •OH radicals gives degradation rates of 31% for ZnO and 31.4% for ZnO/rGO. These degradation rates are less than the 100%

degradation rate observed in the absence of scavengers, as displayed in Figure 11. This experiment highlights the principal role of •OH radicals in the degradation of MB dye.

Moreover, the use of ethylenediaminetetraacetic acid (EDTA) as a scavenger for hydrogen ions (h^+) led to a degradation rate of 33% for ZnO and 38% for ZnO/ rGO, demonstrating the substantial contribution of h^+ ions in the MB photodegradation process. In addition, the use of $K_2Cr_2O_7$ as a scavenger gives a degradation rate of 59.2% for ZnO, suggesting a significant contribution of electron (e^-) species in the degradation mechanism. Moreover, it was observed that the degradation rate of ZnO/rGO was 11%, indicating that the participation of electrons is the primary factor in the degradation of MB when ZnO/rGO is involved in the process.

The significant difference in response in the presence of e-scavengers between the two systems is attributable to distinct degradation mechanisms between ZnO and the ZnO/rGO composite. ZnO, as an efficient photocatalyst exposed to UV light, generates electron-hole pairs, producing reactive oxygen species such as hydroxyl radicals (•OH) and superoxides ($O2^{•-}$). However, ZnO can also produce free electrons that react with oxygen species, generating reducing radicals that act as scavengers, neutralizing undesirable reactive species. In contrast, the ZnO/rGO composite integrates the photocatalytic properties of ZnO with the conductivity of reduced graphene oxide (rGO). The rGO acts as an electron acceptor, promoting the effective separation of electron–hole pairs generated during photocatalysis. In the presence of rGO, the recombination of electrons and holes is reduced, thereby enhancing the overall efficiency of the photocatalytic process.

2.5. Degradation Kinetic Modeling

To investigate the kinetics of chemical pollutant degradation, it is essential to monitor how concentration changes over time in the outlet of a reactor. This involves conducting experiments with various initial concentrations of the pollutant. The apparent kinetic constants, denoted as kapp, are achieved by analyzing the plot depicting the natural logarithm of the ratio of the current concentration to the initial concentration ($Ln(C/C_o)$) as a function of time (Figure 12) [46].
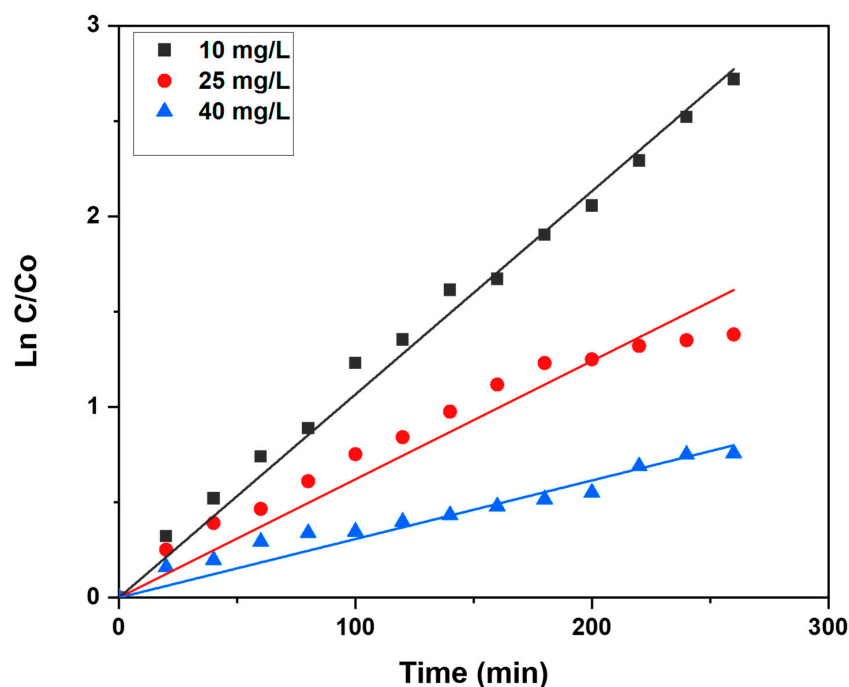

Figure 12. Pseudo-first-order apparent constant values for the different initial concentrations of MB.

The initial rate of the degradation reaction, denoted as r_o, can be calculated using the obtained kapp values and the initial concentration (C_o) of the pollutant. The equation for

this calculation is $r_o = k_{app} * C_o$. This relationship helps in the characterization of the initial rate at which the pollutant is being degraded and provides valuable insights into the kinetics of the chemical reaction.

Photocatalysis is one form of heterogeneous catalysis involving an electron transfer process, commonly described by the Langmuir–Hinshelwood (L-H) model. The Langmuir–Hinshelwood kinetic model is extensively employed to elucidate the kinetics governing the photocatalytic oxidation of organic pollutants. This model provides a framework for quantifying the rate of degradation of an organic pollutant under varying concentrations [47].

The reaction rate can be mathematically represented as:

$$r = -\frac{dc}{dt} = \frac{kr \cdot KC}{1 + KC} \tag{3}$$

The inverse of the equation leads to

$$\frac{1}{r_0} = \frac{1}{kr} + \frac{1}{kr \cdot K} \cdot \frac{1}{C_0} \tag{4}$$

By graphically representing this equation (Figure 13), we can determine the kinetic constants of the Langmuir–Hinshelwood model.
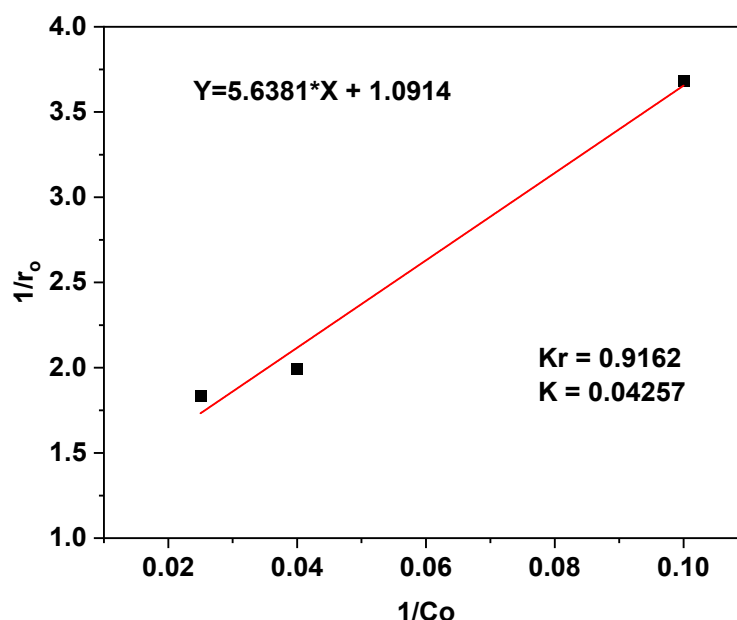

Figure 13. Langmuir–Hinshelwood kinetic plot for the photocatalytic decolorization of methyl blue.

The calculated constants from the Langmuir–Hinshelwood model are $k_r = 0.9162$ mg/L and $K = 0.04257$ L/mg. It can be observed that kr is greater than K, indicating the differences between the photoabsorption and photodegradation reactions. According to the findings of this kinetic study, the Langmuir–Hinshelwood model is confirmed in the MB photodegradation.

2.6. Proposed Photodegradation Mechanism

The photodegradation mechanism of MB using a ZnO/rGO nanocomposite under UV light involves a series of intricate steps. When exposed to UV light, ZnO nanoparticles absorb photons, leading to the generation of electron–hole pairs ($e^- - h^+$) due to bandgap excitation [48]. These excited electrons migrate to the nearby rGO sheets, preventing recombination with holes and enhancing their mobility. Simultaneously, MB ionic molecules

in the solution are adsorbed onto the ZnO/rGO composite surface through electrostatic interactions [49].

$$ZnO + UV\ light \rightarrow ZnO^*\ (excited) + e^- + h^+ \tag{5}$$

$$e^-\ (on\ ZnO^*) \rightarrow e^-\ (on\ rGO) \tag{6}$$
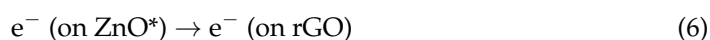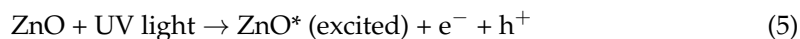
The photocatalytic degradation process begins as the excited electrons on the rGO sheets participate in redox reactions with adsorbed oxygen species (O_2) or hydroxyl ions (OH^-) present in water, yielding superoxide radicals ($\bullet O_2^-$) and hydroxyl radicals ($\bullet OH$) [50]. These reactive radicals are highly oxidative and initiate attacks on the adsorbed MB molecules, breaking them down into smaller, less colored fragments.

$$e^-\ (on\ rGO) + O_2 \rightarrow \bullet O_2^- \tag{7}$$

$$e^-\ (on\ rGO) + H_2O \rightarrow \bullet OH \tag{8}$$

As this degradation process continues, MB molecules are progressively transformed into non-toxic byproducts, such as carbon dioxide and water.

(a) Oxidation by superoxide radicals: $\bullet O_2^-$ attacks MB, causing its breakdown:

$$\bullet O_2^- + MB\ (on\ ZnO/rGO) \rightarrow Degraded\ Products \tag{9}$$

(b) Oxidation by hydroxyl radicals: $\bullet OH$ radicals also attack MB, further breaking it down:

$$\bullet OH + MB\ (on\ ZnO/rGO) \rightarrow Degraded\ Products \tag{10}$$

Throughout this cycle, electrons return to the ZnO nanoparticles to fill the electron vacancies (holes) created during the initial excitation, facilitating the sustained photocatalytic activity of the composite [51].

$$^+ + e^-\ (on\ rGO) \rightarrow ZnO \tag{11}$$

This detailed mechanism underscores the synergistic actions of ZnO and rGO in harnessing UV light for the efficient degradation of MB, with ZnO serving as the photocatalyst and rGO enhancing electron transfer and minimizing electron–hole recombination, resulting in the effective removal of organic pollutants from the solution. Figure 14 summarizes the degradation mechanism.
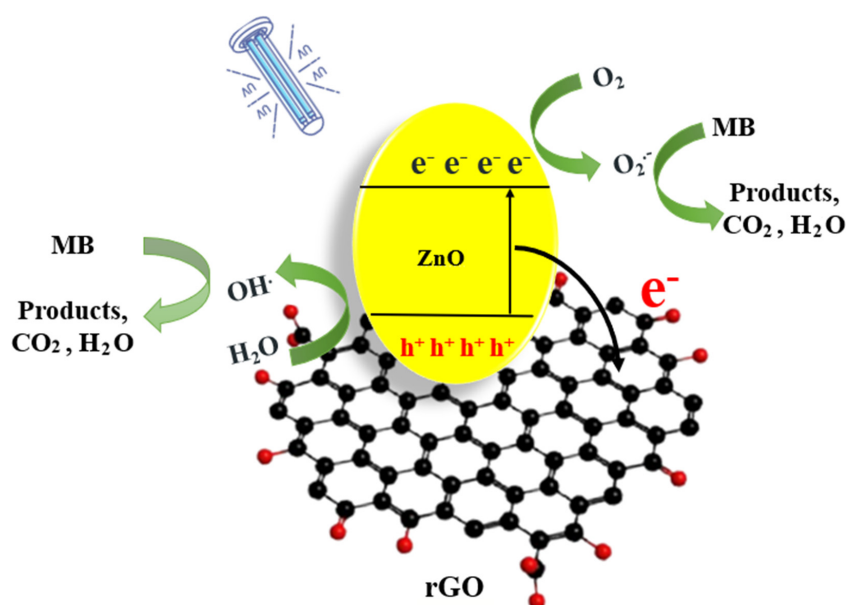

Figure 14. The photodegradation mechanism of methylene blue.

2.7. Comparison of the Photocatalytic Efficacy of Commercial TiO$_2$ P25 and ZnO Nanoparticles Synthetized by Different Methods

A thorough comparative analysis was conducted to assess the photodegradation efficiency of ZnO-NPs) relative to TiO2 P25. The detailed results, outlined in Table 6, cover a comprehensive examination of ZnO-NPs prepared through various alternative methods. Notably, previously documented ZnO-NP catalysts employed diverse synthesis approaches, with a particular focus on biological methods. The evaluation of their photocatalytic activity involved the use of MB as the selected dye, contributing a valuable dimension to the multifaceted exploration of catalyst performance.

Table 6. Comparison of the photocatalytic efficacy of commercial TiO$_2$ P25 and ZnO nanoparticles.

Catalyst	Preparation Method/Plant	Dye	Irradiation	Particle Size (nm)	Irradiation Time/min	Catalyst Dose/g L^{-1}	Dye Conc./ mg L^{-1}	Degradation Efficiency/%	Ref.
P25 Degussa		MB	UV lamp	<21	60	1	10	41	[52]
ZnO@OFE	Biosynthesis *O. europaea*	MB	Sunlight	24.3	180	1	10	75	[53]
ZnO	Sol gel	MB	UV (Hg lamp 365 nm)	25	120	0.33	10	37	[54]
ZnO	Biosynthesis/ *Syzygium cumini*	MB	UV (365 nm)	25–30	60	2	1–2	84	[55]
ZnO-Bi$_2$O$_3$	Co-precipitation	RO16	UV lamp	29.6	100	0.2	100	28	[56]
ZnO	Biosynthesis/ Date Syrup	MB	UV lamp	14	140	1	10	86.6	Present work
ZnO/rGO	Hydrothermal	MB	UV lamp	20	140	1	10	100	This work

Table 6 unfolds a comprehensive panorama of catalysts sourced from diverse studies, providing nuanced insights into their unique photodegradation efficiencies. Amidst this varied array, our ZnO nanoparticles, intricately synthesized through a distinctive biological process involving Date Syrup, emerge as beacons of excellence. Their extraordinary efficacy is accentuated when juxtaposed with other materials scrutinized in separate investigations.

A meticulous exploration of the entries reveals intriguing dynamics. For example, the initial catalyst, P25 Degussa, showcased a 41% degradation efficiency under UV lamp irradiation. In stark contrast, ZnO@OFE, synthesized via biosynthesis from Olea europaea, demonstrated a significantly higher efficiency of 75% under sunlight exposure, underscoring the inherent advantages of employing biologically synthesized ZnO nanoparticles, especially in harnessing solar energy for effective photocatalysis.

Delving deeper into the entries, which include ZnO synthesized through sol–gel and various biosynthetic methods, such as those incorporating *Syzygium cumini* and Date Syrup, reveals a captivating spectrum of particle sizes, irradiation times, and degradation efficiencies. For instance, ZnO synthesized through sol–gel methods showcased a degradation efficiency of 37%, employing UV (Hg lamp 365 nm) irradiation. Additionally, ZnO synthesized via biosynthesis from *Syzygium cumini* exhibited a particle size range of 25–30 nm, an irradiation time of 60 min, and achieved a degradation efficiency of 84% (the initial concentration of MB was 2 mg/L) under UV (365 nm) irradiation. Furthermore, the table includes entries like ZnO-Bi$_2$O$_3$, synthesized through co-precipitation using RO16 as the dye, with a particle size of 29.6 nm, an irradiation time of 100 min, and a remarkable degradation efficiency of 28%. It is essential to note that despite ZnO-Bi$_2$O$_3$ degrading 28 mg/L of RO16, this does not necessarily imply superiority to our material. This is because MB is often considered relatively stable and persistent, potentially making its degradation more challenging compared to RO16.

The standout contribution of our study becomes evident when scrutinizing the ZnO nanoparticles synthesized with Date Syrup. Boasting an impressive degradation efficiency of 86.6% under UV lamp irradiation for 140 min, our catalyst surpasses its ZnO counterparts in the Table 6. Furthermore, the hydrothermally synthesized ZnO/rGO composite in our study emerges as a pinnacle of photocatalytic capability, achieving a complete degradation efficiency of 100%.

In essence, our comparative analysis not only underscores the superior photodegradation efficiency of our ZnO nanoparticles, particularly those synthesized with Date Syrup, but also positions them as promising candidates for diverse applications in photocatalysis. Beyond the numerical outcomes, the richness of this exploration lies in the diverse synthesis methods employed, offering broader implications for the potential utilization of ZnO nanoparticles in various environmental and industrial contexts.

3. Materials and Methods

3.1. Materials

The materials used included Algerian Date Syrup (Molasses), zinc acetate dihydrate ($(CH_3COO)_2Zn \cdot 2H_2O$) from ISOLAB (Eschau, Germany), graphene from Sigma Aldrich (St. Louis, MO, USA), and sodium hydroxide and hydrochloric acid HCl (37%) from Scharlau (Barcelona, Spain). Ethanol and methanol were sourced from BIOCHEM (Cosne-Cours-sur-Loire, France), while methylene blue (MB) (Sigma Aldrich) served as a model pollutant. All chemicals utilized in the study met analytical reagent grade standards and they were used without the need for any further purification.

3.2. Methods

3.2.1. Algerian Date Syrup (Molasses) Extract Preparation

For this preparation, we opted to use industrial date molasses from the SALAMA brand sourced from the Biskra region in the southeast of Algeria. To ensure the standardization of the physicochemical parameters of our extract, employed in the synthesis of zinc oxide (ZnO), a comprehensive series of physicochemical characterizations was undertaken according to precise standards and analytical methods. The moisture content, assessed following the protocol by Reynes et al. [57], revealed a concentration of 26.18%, indicating a notably thick consistency of the syrup. The pH, determined in accordance with (AFNOR NF V 5 V 50-108) [58], registered an acidic value of 5.3, necessitating adjustment during the ZnO synthesis. Total sugars, evaluated using the Dubois phenol method [59], comprised a substantial proportion of 60.28%. Reducing sugars, quantified through colorimetry using the Miller method [60], reached 29.9%, justifying our decision to work with date syrup extract due to their pivotal role in reducing metal ions. The sucrose content, computed as the difference between total sugars and reducing sugars [61], amounted to 30.31%. Protein content, measured via the Kjeldahl method following AOAC 1995 standards [62], was relatively low at 0.42% compared to other constituents. Total polyphenols, as determined by the method of Juntachote et al. [63], revealed a significant concentration of 29.57 mg/100 g, underscoring the antioxidant properties of these compounds as reducing agents. Finally, the estimation of total flavonoids in the molasses, conducted following the method described by Gursoy et al. [64], yielded a value of 8.08 mg/100 g. These nuanced results contribute to an enriched understanding of the fundamental components of date molasses and their potential as effective reducing agents in the environmentally friendly synthesis of ZnO.

To make the extract, 20 g of date molasses was dispersed in 200 mL of distilled water. The mixture was then heated to 60 °C for 20 min under stirring until all the date molasses was evenly mixed. After heating, the solution was allowed to cool and filtered using Whatman filter paper, and the filtrate was collected. Subsequently, the resulting filtrate was used as a stock solution for the synthesis of ZnO nanoparticles as shown in Figure 15.
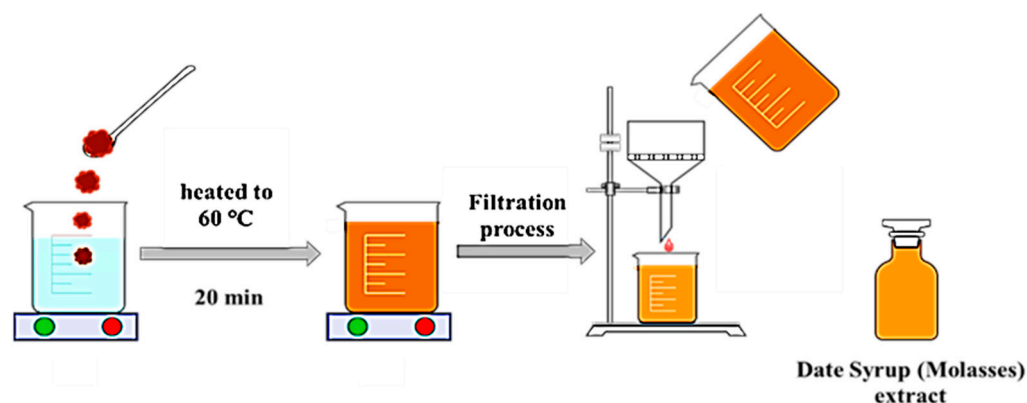
Figure 15. Algerian Date Syrup (Molasses) extract preparation.

3.2.2. Synthesis of ZnO NPs

The synthesis of ZnO nanoparticles was meticulously initiated by the gradual addition of 20 mL of the extract into an 80 mL solution of 0.1 M zinc acetate. The reaction vessel was maintained at a precise temperature of 90 °C, and the mixture was subjected to stirring at 700 rpm to ensure homogeneity. Upon achieving the designated temperature, a NaOH solution was delicately introduced dropwise into the reaction mixture. This marked the commencement of a carefully monitored 4 h aging process, during which a remarkable transformation occurred—the solution's initial brown hue evolved into a pristine white, indicative of the formation of the desired precipitate.

Following this intriguing phase, ultrasonic treatment was meticulously applied for 60 min. This step was crucial for further enhancing the homogeneity and structural integrity of the synthesized ZnO nanoparticles. The resulting solution, now rich in well-formed nanoparticles, underwent a precision-controlled centrifugation process at 3600 rpm for 30 min. This step was imperative for efficiently collecting the synthesized ZnO nanoparticles, as the centrifugal force facilitated the separation of the nanoparticles from the remaining solution.

To ensure the purity of the synthesized nanoparticles, they were subjected to a meticulous purification process. The collected ZnO NPs were suspended in a carefully crafted mixture of ethanol and distilled water. This purification step aimed to eliminate any impurities or unreacted substances that might have been present in the solution. The suspension was then subjected to controlled conditions, allowing for the removal of solvent through air drying at 60 °C in a vacuum oven overnight. The resulting dried powder, rich in synthesized ZnO nanoparticles, was delicately collected for further characterization.

In the subsequent phase, the collected sample underwent a thermal treatment process known as calcination. This involved subjecting the sample to varying temperatures, specifically 450 °C, 550 °C, and 600 °C. The selection of these temperatures was based on a comprehensive understanding of the desired structural and chemical properties of the ZnO nanoparticles. The thermal treatment was meticulously illustrated in Figure 16, providing a visual representation of the temperature-dependent transformations and the resultant characteristics of the synthesized nanoparticles.

Phenolic compounds contribute to reducing and stabilizing properties, while natural antioxidants help maintain the stability of nanoparticles. Minerals and trace elements in date molasses could also influence the growth and properties of ZnO nanoparticles. In the absence of molasses, the reduction process could face impediments, potentially compromising the efficiency of ZnO nanoparticle synthesis. Molasses, with its organic diversity, emerges as an environmentally friendly alternative, offering a sustainable approach that replaces traditional chemical reducing agents with notable advantages in terms of both efficiency and ecological impact. The incorporation of molasses aligns with a green synthesis approach, emphasizing the eco-friendly nature of our methodology.
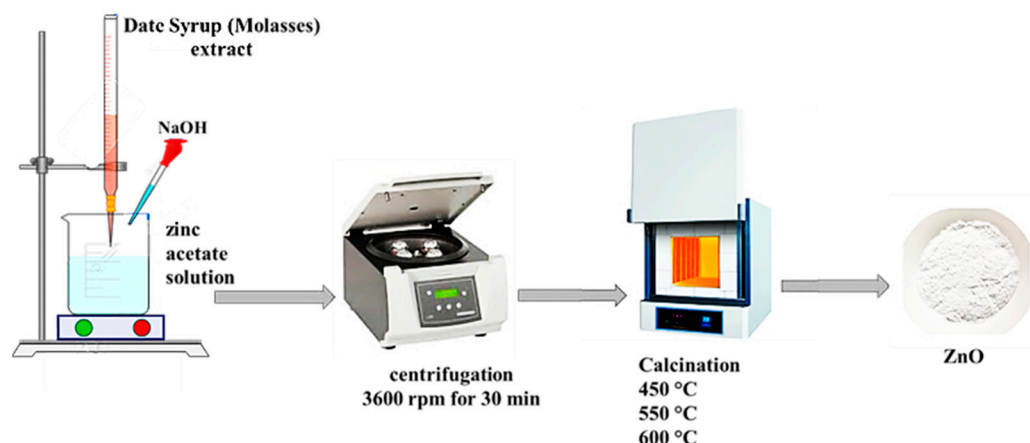
Figure 16. Schematic presentation of ZnO green synthesis. The incorporation of molasses in our synthesis process holds paramount importance, as its richness in diverse compounds offers various possibilities in ZnO synthesis. Natural sugars present, such as glucose, fructose, and sucrose, can act as reducing agents.

3.2.3. Preparation of ZnO/rGOx Photocatalysts

ZnO/rGOx photocatalysts were synthesized using a hydrothermal method through varying the weight ratios of rGO to ZnO at 5%, 10%, and 15% by weight of rGO to ZnO. In this process, 1 g of ZnO powder and an appropriate mass percentage of graphene were dispersed in a solution of double-distilled water and ethanol, and the obtained mixture was treated for 1 h in an ultrasonic bath and stirred for another 2 h to obtain homogeneous suspension. The resulting suspension was then placed in a Teflon-sealed autoclave and kept for 12 h at 120 °C. The resulting product was washed four times using a combination of distilled water and ethanol using a centrifuge and dried in an oven at 65 °C for 24 h in the manner indicated by the diagram (Figure 17).
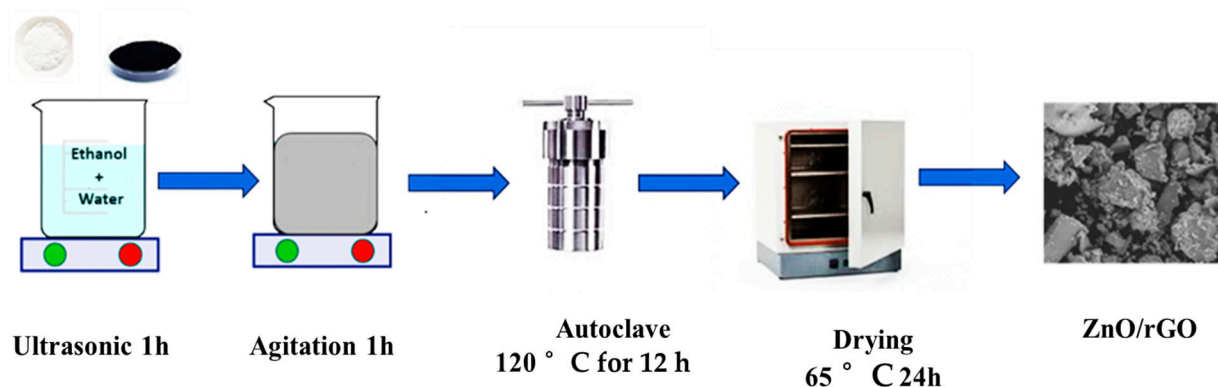

Figure 17. Schematic diagram for preparing the ZnO/rGO$_x$ nanocomposites.

3.3. Characterization

X-ray diffraction (XRD) analysis of the samples was conducted using a Bruker D2 PHASER diffractometer located in Karlsruhe, Germany. For each dry powdered sample, the instrument scanned and recorded diffraction patterns within the angular range of 15° to 80° (2θ). For the morphological evaluation of ZnO and ZnO/rGO nanocomposites, scanning electron microscopy (SEM) was employed. The analysis took place at a temperature of 25 °C and utilized a Scanning Electron Microscope (FEI Quanta 250, Hillsboro,. OR, USA) connected to xT microscopy software for data analysis. All samples were observed under an accelerating potential of 15 kV, with magnifications of $3000\times g$ and $6000\times g$. The IR spectra of the ligands and the synthesized complexes in this study were obtained using a

Perkin Elmer FTIR Fourier-transform infrared (Waltham, MA, USA) spectrometer in the range of 4000–400 cm^{-1} with a spectral resolution of 4 cm^{-1}, utilizing the Attenuated Total Reflection (ATR) technique. The investigation of photocatalysis involved the utilization of a Shimadzu 1700 UV-Vis (Tokyo, Japan) spectrophotometer to ascertain the concentration of MB. Spectral data were collected within the wavelength range of 200 to 800 nm, and kinetic profiles were constructed by tracking the absorbance at the maximum wavelength (λmax) of 663 nm for MB.

3.4. Photocatalytic Degradation Studies of Methylene Blue

The photocatalytic experiments were meticulously conducted in a batch photoreactor at room temperature, utilizing Philips UV PL-L 24 W lamps (Amsterdam, The Netherlands) that emit light with a peak wavelength of 253.7 nm. These lamps were strategically positioned 5 cm above a graduated cylinder. MB was chosen as the model molecule owing to its widespread availability and extensive application in various industries, a selection motivated by several compelling factors.

MB, distinguished by its vivid and distinctive color, serves as a practical aid for visually tracking changes during photodegradation. Its inherent photosensitivity and chemical reactivity to light make it an ideal indicator for probing photodegradation processes. The well-documented photodegradation properties of MB not only render it a reliable model for scrutinizing photochemical degradation mechanisms but also allow for the extrapolation of insights gained to enhance our understanding of other compounds. Its ubiquity across diverse scientific disciplines establishes MB as a favored choice for photodegradation tests, underscoring its versatility as a preferred tool for researchers working with varied compound types. Furthermore, the economic feasibility of MB adds to its appeal as a cost-effective option for laboratory experiments.

The determination of MB concentration variations relied on the peak at 663 nm, derived from the calibration curve. The experimental protocol involved dispersing 1 g/L of ZnO/rGOx (x = 0, 5, 10, and 15%) in 100 mL of an aqueous MB solution (10 mg/L). Initially, the solution underwent stirring in darkness for 40 min to attain adsorption–desorption equilibrium. Subsequently, the UV lamp was activated, and at 20 min intervals, 1 mL of the suspension was withdrawn (dilutions × 3) and promptly centrifuged to separate the catalyst from the solution. The resulting solution underwent analysis by UV-Vis spectroscopy. To ensure the photostability of the photocatalyst, all experiments were conducted in triplicate. The color removal efficiency was determined using the formula:

$$\text{Color removal efficiency } (\%) = \frac{C_o - C_e}{C_o} \times 100 \tag{12}$$

where C_o is the initial MB concentration (mg/L) and C_e is the MB concentration at the time t (mg/L).

The reaction kinetics of photocatalytic degradation was investigated using the Langmuir–Hinshelwood kinetic model for organic compound degradation.

$$-\text{Ln}(C/C_o) = kt \tag{13}$$

where C_o is the initial concentration, C is the measured concentration at the time t (min), and k is the apparent kinetic constant (min^{-1}), which is measured from the slope of the linear fitting line.

4. Conclusions

The success of the new biosynthesis of zinc oxide nanoparticles (ZnO-NPs) was achieved using an aqueous extract of Algerian Date Syrup (molasses). This research delved into determining the optimal calcination temperature of ZnO NPs. To boost the photocatalytic activity of zinc oxide, ZnO/rGOx nanocomposites were prepared through the hydrothermal method, with various percentages of rGO (5%, 10%, and 15%). The chemical,

optical, and morphological characteristics of these composites were extensively examined using SEM, UV DRS, FTIR, and XRD analyses. Furthermore, the photodegradation potential of ZnO NPs and ZnO/rGOx was assessed as a low-cost, environmentally friendly photocatalyst for wastewater treatment. The degradation of MB under UV irradiation was monitored, measuring the absorbance of the decolorization dye solution. Notably, when 1 g/L of ZnO NPs or ZnO/rGO were employed, it resulted in an 86.6% degradation efficiency of the MB solution during 140 min under UV irradiation, underscoring the high potential of ZnO NPs as an effective photocatalyst. Remarkably, the degradation rate soared to 100% when using the ZnO/rGO catalyst within the same time frame, establishing it as the superior photocatalyst for achieving maximum MB dye degradation. Additionally, the investigation examined variables affecting the photocatalytic experiment, encompassing pH levels and the quantity of the catalyst. The results revealed that the ZnO/rGO photocatalyst displayed its peak photocatalytic performance under neutral pH conditions and when used at a concentration of 1 g/L. The stability and recyclability of ZnO/rGO 10% were demonstrated through five consecutive cycles of MB degradation, highlighting its potential for practical applications. Scavenger experiments provided insights into the dominant species involved in the photocatalytic degradation process, with hydroxyl radicals (•OH) and electrons (e^-) playing significant roles. The kinetic modeling, based on pseudo-first-order and Langmuir–Hinshelwood models, further elucidated the degradation kinetics and confirmed the applicability of the Langmuir–Hinshelwood model to the MB photodegradation process. The proposed photodegradation mechanism outlined the synergistic actions of ZnO and rGO, where ZnO served as the photocatalyst, and rGO enhanced electron transfer, minimizing electron–hole recombination. This comprehensive study provides valuable insights into the design and optimization of ZnO/rGO nanohybrids for efficient photocatalytic applications, with potential implications for environmental remediation and wastewater treatment.

Author Contributions: Conceptualization, K.M., D.C., H.A.Y., H.T., A.B., M.K., J.Z. and A.A.; Methodology, K.M., D.C., H.A.Y., H.T., A.B., J.Z. and A.A.; Software, K.M., D.C., H.T., M.K., J.Z. and A.A.; Validation, K.M., D.C., H.A.Y., H.T., A.B., M.K., J.Z. and A.A.; Formal analysis, K.M., D.C., H.A.Y., H.T., A.B., M.K. and A.A.; Investigation, K.M., D.C., H.A.Y., H.T., A.B., M.K., J.Z. and A.A.; Resources, K.M., D.C., H.T., A.B., M.K., J.Z. and A.A.; Data curation, K.M., D.C., A.B., J.Z. and A.A.; Writing—original draft, K.M.; Writing—review and editing, D.C., H.A.Y., H.T., A.B., M.K., J.Z. and A.A.; Visualization, K.M., D.C., H.A.Y., H.T., A.B., M.K., J.Z. and A.A.; Supervision, D.C., H.A.Y., J.Z. and A.A.; Project administration, D.C., J.Z. and A.A. All authors have read and agreed to the published version of the manuscript.

Data Availability Statement: All relevant data is included within the article.

Conflicts of Interest: The authors declare no conflicts of interest.

References

1. Kuspanov, Z.; Bakbolat, B.; Baimenov, A.; Issadykov, A.; Yeleuov, M.; Daulbayev, C. Photocatalysts for a sustainable future: Innovations in large-scale environmental and energy applications. *Sci. Total Environ.* **2023**, *885*, 163914. [CrossRef] [PubMed]
2. Guediri, M.K.; Chebli, D.; Bouguettoucha, A.; Bourzami, R.; Amrane, A. Interfacial coupling effects on adsorptive and photocatalytic performances for photoresponsive graphene-wrapped SrTiO3@Ag under UV–visible light: Experimental and DFT approach. *Environ. Sci. Pollut. Res.* **2022**, *29*, 28098–28114. [CrossRef] [PubMed]
3. Khan, I.; Saeed, K.; Khan, I. Nanoparticles: Properties, applications and toxicities. *Arab. J. Chem.* **2019**, *12*, 908–931. [CrossRef]
4. Tahir, M.B.; Sohaib, M.; Sagir, M.; Rafique, M. Role of Nanotechnology in Photocatalysis. In *Encyclopedia of Smart Materials*; Elsevier: Amsterdam, The Netherlands, 2021; pp. 578–589. [CrossRef]
5. Pal, G.; Rai, P.; Pandey, A. *Green Synthesis of Nanoparticles: A Greener Approach for a Cleaner Future*; Elsevier: Amsterdam, The Netherlands, 2019; pp. 1–26. [CrossRef]
6. Alsaiari, N.S.; Alzahrani, F.M.; Amari, A.; Osman, H.; Harharah, H.N.; Elboughdiri, N.; Tahoon, M.A. Plant and Microbial Approaches as Green Methods for the Synthesis of Nanomaterials: Synthesis, Applications, and Future Perspectives. *Molecules* **2023**, *28*, 463. [CrossRef] [PubMed]

7. Baig, N.; Kammakakam, I.; Falath, W. Nanomaterials: A review of synthesis methods, properties, recent progress, and challenges. *Mater. Adv.* **2021**, *2*, 1821–1871. [CrossRef]

8. Klinbumrung, A.; Panya, R.; Pung-Ngama, A.; Nasomjai, P.; Saowalakmeka, J.; Sirirak, R. Green synthesis of ZnO nano-particles by pineapple peel extract from various alkali sources. *J. Asian Ceram. Soc.* **2022**, *10*, 755–765. [CrossRef]

9. Javed, M.N.; Bangash, S.A.K.; Abbas, M.; Ahmed, S.; Kaplan, A.; Iqbal, S.; Wahab, S. Potential and Challenges in Green Synthesis of Nanoparticles: A Review. *Xi'an Shiyou Daxue Xuebao (Ziran Kexue Ban)/J. Xi'an Shiyou Univ.* **2023**, *19*, 1155–1165.

10. Kulkarni, D.; Sherkar, R.; Shirsathe, C.; Sonwane, R.; Varpe, N.; Shelke, S.; More, M.P.; Pardeshi, S.R.; Dhaneshwar, G.; Junnuthula, V.; et al. Biofabrication of nanoparticles: Sources, synthesis, and biomedical applications. *Front. Bioeng. Biotechnol.* **2023**, *11*, 1159193. [CrossRef]

11. Balkrishna, A.; Kumar, A.; Arya, V.; Rohela, A.; Verma, R.; Nepovimova, E.; Krejcar, O.; Kumar, D.; Thakur, N.; Kuca, K. Phytoantioxidant Functionalized Nanoparticles: A Green Approach to Combat Nanoparticle-Induced Oxidative Stress. *Oxidative Med. Cell. Longev.* **2021**, *2021*, 1–20. [CrossRef]

12. Kumar, H.; Bhardwaj, K.; Kuča, K.; Kalia, A.; Nepovimova, E.; Verma, R.; Kumar, D. Flower-Based Green Synthesis of Metallic Nanoparticles: Applications beyond Fragrance. *Nanomaterials* **2020**, *10*, 766. [CrossRef]

13. Alhuzali, S.M.A.; Jibrin, N.M.H.; Aljaber, R.J.A.; Albisher, A.O.M. Dates palm (*Phoenix dactylifera* L.) Fruits: Nutritional Properties and Potential Applications. المجلة العربية للعلوم الزراعية **2023**, *17*, 137–160. [CrossRef]

14. Rambabu, K.; Bharath, G.; Banat, F.; Show, P.L. Green synthesis of zinc oxide nanoparticles using *Phoenix dactylifera* waste as bioreductant for effective dye degradation and antibacterial performance in wastewater treatment. *J. Hazard. Mater.* **2020**, *402*, 123560. [CrossRef]

15. Subhan, A.; Neogi, N.; Choudhury, K.P. Industrial Manufacturing Applications of Zinc Oxide Nanomaterials: A Comprehensive Study. *Nanomanufacturing* **2022**, *2*, 265–291. [CrossRef]

16. Thakur, K.; Kandasubramanian, B. Graphene and Graphene Oxide-Based Composites for Removal of Organic Pollutants: A Review. *J. Chem. Eng. Data* **2019**, *64*, 833–867. [CrossRef]

17. Al-Marri, A.H.; Janene, F.; Moulahi, A.; Mogharbel, A.T.; Al-Farraj, E.S.; Al-Mohaimeed, A.M.; Mjejri, I. Enhanced photocatalytic properties of the Nb_2O_5/rGO for the degradation of methylene blue. *Ionics* **2023**, *29*, 5505–5515. [CrossRef]

18. Pu, Y.-C.; Chou, H.-Y.; Kuo, W.-S.; Wei, K.-H.; Hsu, Y.-J. Interfacial charge carrier dynamics of cuprous oxide-reduced graphene oxide (Cu2O-rGO) nanoheterostructures and their related visible-light-driven photocatalysis. *Appl. Catal. B Environ.* **2017**, *204*, 21–32. [CrossRef]

19. Bagheri, S.; Esrafili, A.; Kermani, M.; Mehralipour, J.; Gholami, M. Performance evaluation of a novel rGO-Fe^0/Fe$_3$O$_4$-PEI nanocomposite for lead and cadmium removal from aqueous solutions. *J. Mol. Liq.* **2020**, *320*, 114422. [CrossRef]

20. Wen, M.Y.S.; Abdullah, A.H.; Ngee, L.H. Sintesis nanohibrid ZnO/rGO untuk mempertingkatkan aktiviti fo-topemangkinan. *Malays. J. Anal. Sci.* **2017**, *21*, 889–900. [CrossRef]

21. Karpuraranjith, M.; Chen, Y.; Manigandan, R.; Srinivas, K.; Rajaboopathi, S. Hierarchical Ultrathin Layered GO-ZnO@CeO$_2$ Nanohybrids for Highly Efficient Methylene Blue Dye Degradation. *Molecules* **2022**, *27*, 8788. [CrossRef]

22. Li, D.; Lu, J.; Zhang, X.; Jin, D.; Jin, H. Engineering of ZnO/rGO towards NO$_2$ Gas Detection: Ratio Modulated Sensing Type and Heterojunction Determined Response. *Nanomaterials* **2023**, *13*, 917. [CrossRef]

23. Nandiyanto, A.B.D.; Zaen, R.; Oktiani, R. Correlation between crystallite size and photocatalytic performance of micrometer-sized monoclinic WO$_3$ particles. *Arab. J. Chem.* **2020**, *13*, 1283–1296. [CrossRef]

24. AbuDalo, M.A.; Al-Mheidat, I.R.; Al-Shurafat, A.W.; Grinham, C.; Oyanedel-Craver, V. Synthesis of silver nanoparticles using a modified Tollens' method in conjunction with phytochemicals and assessment of their antimicrobial activity. *PeerJ* **2019**, *7*, e6413. [CrossRef]

25. Matar, H.A.; Ibrahim, M.A.; El-Hagary, M. Simple and cost-effective route for PANI-ZnO-rGO nanocomposite as a biosensor for L-arginine detection. *Diam. Relat. Mater.* **2023**, *133*, 109703. [CrossRef]

26. Souri, M.; Ghaemi, N.; Shakeri, A.; Hoseinpour, V. Optimization of green synthesis of ZnO nanoparticles by *Dittrichia graveolens* (L.) aqueous extract. *Health Biotechnol. Biopharma* **2017**, *1*, 39–49. [CrossRef]

27. Alzahrani, E.A.; Nabi, A.; Kamli, M.R.; Albukhari, S.M.; Althabaiti, S.A.; Al-Harbi, S.A.; Khan, I.; Malik, M.A. Facile Green Synthesis of ZnO NPs and Plasmonic Ag-Supported ZnO Nanocomposite for Photocatalytic Degradation of Methylene Blue. *Water* **2023**, *15*, 384. [CrossRef]

28. De Peres, M.L.; Delucis, R.d.A.; Amico, S.C.; Gatto, D.A. Zinc oxide nanoparticles from microwave-assisted solvothermal process: Photocatalytic performance and use for wood protection against xylophagous fungus. *Nanomater. Nanotechnol.* **2019**, *9*, 1847980419876201. [CrossRef]

29. Christobel, G.J. Vibrational Spectroscopy of ZnO-ZnS Nanoparticles. *Int. J. Sci. Res.* **2013**, *5*, 2013. [CrossRef]

30. Khan, S.H.; R, S.; Pathak, B.; Fulekar, M. Photocatalytic degradation of organophosphate pesticides (Chlorpyrifos) using synthesized zinc oxide nanoparticle by membrane filtration reactor under UV irradiation. *Front. Nanosci. Nanotechnol.* **2015**, *1*, 23–27. [CrossRef]

31. Jaramillo-Páez, C.; Navío, J.; Hidalgo, M.; Macías, M. ZnO and Pt-ZnO photocatalysts: Characterization and photocatalytic activity assessing by means of three substrates. *Catal. Today* **2018**, *313*, 12–19. [CrossRef]

32. Misra, K.P.; Kumawat, A.; Kumari, P.; Samanta, S.; Halder, N.; Chattopadhyay, S. Band Gap Reduction and Petal-like Nanostructure Formation in Heavily Ce-doped ZnO Nanopowders. *J. Nano- Electron. Phys.* **2021**, *13*, 02008. [CrossRef]

33. Üstün, E.; Önbaş, S.C.; Çelik, S.K.; Ayvaz M, Ç.; Şahin, N. Green Synthesis of Iron Oxide Nanoparticles by Using Ficus Carica Leaf Extract and Its Antioxidant Activity. *Biointerface Res. Appl. Chem.* **2021**, *12*, 2108–2116. [CrossRef]

34. Chandrappa, K.G.; Venkatesha, T.V. Electrochemical Synthesis and Photocatalytic Property of Zinc Oxide Nanoparticles. *Nano-Micro Lett.* **2012**, *4*, 14–24. [CrossRef]

35. Sharma, V.; Sharma, J.; Kansay, V.; Sharma, V.D.; Sharma, A.; Kumar, S.; Bera, M. The effect of calcination temperatures on the structural and optical properties of zinc oxide nanoparticles and their influence on the photocatalytic degradation of leather dye. *Chem. Phys. Impact* **2023**, *6*, 100196. [CrossRef]

36. Tien, H.N.; Luan, V.H.; Hoa, L.T.; Khoa, N.T.; Hahn, S.H.; Chung, J.S.; Shin, E.W.; Hur, S.H. One-pot synthesis of a reduced graphene oxide–zinc oxide sphere composite and its use as a visible light photocatalyst. *Chem. Eng. J.* **2013**, *229*, 126–133. [CrossRef]

37. Xu, S.; Fu, L.; Pham, T.S.H.; Yu, A.; Han, F.; Chen, L. Preparation of ZnO flower/reduced graphene oxide composite with enhanced photocatalytic performance under sunlight. *Ceram. Int.* **2015**, *41*, 4007–4013. [CrossRef]

38. Liu, H.R.; Shao, G.X.; Zhao, J.F.; Zhang, Z.X.; Zhang, Y.; Liang, J.; Liu, X.G.; Jia, H.S.; Xu, B.S. Worm-Like Ag/ZnO Core–Shell Heterostructural Composites: Fabrication, Characterization, and Photocatalysis. *J. Phys. Chem. C* **2012**, *116*, 16182–16190. [CrossRef]

39. Fang, J.; Fan, H.; Dong, G. A facile way to synthesize cost-effective ZnO nanorods with enhanced photocatalytic activity. *Mater. Lett.* **2014**, *120*, 147–150. [CrossRef]

40. Guediri, M.K.; Chebli, D.; Bouguettoucha, A.; Bourzami, R.; Amrane, A. Novel Fe_2TiO_5/reduced graphene oxide heterojunction photocatalyst with improved adsorption capacity and visible light photoactivity: Experimental and DFT approach. *Environ. Sci. Pollut. Res.* **2020**, *28*, 8507–8519. [CrossRef] [PubMed]

41. Kaus, N.H.M.; Rithwan, A.F.; Adnan, R.; Ibrahim, M.L.; Thongmee, S.; Yusoff, S.F.M. Effective Strategies, Mechanisms, and Photocatalytic Efficiency of Semiconductor Nanomaterials Incorporating rGO for Environmental Contaminant Degradation. *Catalysts* **2021**, *11*, 302. [CrossRef]

42. Garg, R.; Gupta, R.; Singh, N.; Bansal, A. Characterization and performance evaluation of synthesized ZnO nanoflowers, nanorods, and their hybrid nanocomposites with graphene oxide for degradation of Orange G. *Environ. Sci. Pollut. Res.* **2021**, *28*, 57009–57029. [CrossRef] [PubMed]

43. Zhou, F.; Yan, C.; Liang, T.; Sun, Q.; Wang, H. Photocatalytic degradation of Orange G using sepiolite-TiO_2 nanocomposites: Optimization of physicochemical parameters and kinetics studies. *Chem. Eng. Sci.* **2018**, *183*, 231–239. [CrossRef]

44. Trenczek-Zajac, A.; Synowiec, M.; Zakrzewska, K.; Zazakowny, K.; Kowalski, K.; Dziedzic, A.; Radecka, M. Scavenger-Supported Photocatalytic Evidence of an Extended Type I Electronic Structure of the TiO_2@Fe_2O_3 Interface. *ACS Appl. Mater. Interfaces* **2022**, *14*, 38255–38269. [CrossRef] [PubMed]

45. Ahmad, R.; Mondal, P.K. Adsorption and Photodegradation of Methylene Blue by Using PAni/TiO_2Nanocomposite. *J. Dispers. Sci. Technol.* **2012**, *33*, 380–386. [CrossRef]

46. Aisien, F.; Amenaghawon, A.N.; Urhobotie, O.I. Potential Application of a Locally Sourced Photocatalyst for the Photocatalytic Decolourisation of Methyl Orange in Aqueous Solution. *J. Eng. Sci. Technol.* **2015**, 1641–1653.

47. Gupta, N.K.; Ghaffari, Y.; Kim, S.; Bae, J.; Kim, K.S.; Saifuddin, M. Photocatalytic Degradation of Organic Pollutants over MFe_2O_4 (M = Co, Ni, Cu, Zn) Nanoparticles at Neutral pH. *Sci. Rep.* **2020**, *10*, 4942. [CrossRef] [PubMed]

48. Raghu, M.; Parashuram, L.; Prashanth, M.; Kumar, K.Y.; Kumar, C.P.; Alrobei, H. Simple in-situ functionalization of polyaniline with boroncarbonitride as potential multipurpose photocatalyst: Generation of hydrogen, organic and inorganic pollutant detoxification. *Nano-Struct. Nano-Objects* **2021**, *25*, 100667. [CrossRef]

49. Sánchez-Albores, R.; Cano, F.J.; Sebastian, P.; Reyes-Vallejo, O. Microwave-assisted biosynthesis of ZnO-GO particles using orange peel extract for photocatalytic degradation of methylene blue. *J. Environ. Chem. Eng.* **2022**, *10*, 108924. [CrossRef]

50. Waghchaure, R.H.; Adole, V.A.; Jagdale, B.S. Photocatalytic degradation of methylene blue, rhodamine B, methyl orange and Eriochrome black T dyes by modified ZnO nanocatalysts: A concise review. *Inorg. Chem. Commun.* **2022**, *143*, 109764. [CrossRef]

51. Ma, S.; Huang, Y.; Hong, R.; Lu, X.; Li, J.; Zheng, Y. Enhancing Photocatalytic Activity of ZnO Nanoparticles in a Circulating Fluidized Bed with Plasma Jets. *Catalysts* **2021**, *11*, 77. [CrossRef]

52. Rodríguez-Cabo, B.; Rodríguez-Palmeiro, I.; Corchero, R.; Rodil, R.; Rodil, E.; Arce, A.; Soto, A. Photocatalytic degradation of methyl orange, methylene blue and rhodamine B with AgCl nanocatalyst synthesised from its bulk material in the ionic liquid [P6 6 6 14]Cl. *Water Sci. Technol.* **2016**, *75*, 128–140. [CrossRef]

53. Ghaffar, S.; Abbas, A.; Naeem-Ul-Hassan, M.; Assad, N.; Sher, M.; Ullah, S.; Alhazmi, H.A.; Najmi, A.; Zoghebi, K.; Al Bratty, M.; et al. Improved Photocatalytic and Antioxidant Activity of Olive Fruit Extract-Mediated ZnO Nanoparticles. *Antioxidants* **2023**, *12*, 1201. [CrossRef] [PubMed]

54. Azarang, M.; Shuhaimi, A.; Yousefi, R.; Jahromi, S.P. One-pot sol–gel synthesis of reduced graphene oxide uniformly decorated zinc oxide nanoparticles in starch environment for highly efficient photodegradation of Methylene Blue. *RSC Adv.* **2015**, *5*, 21888–21896. [CrossRef]

55. Gawade, V.V.; Sabale, S.R.; Dhabbe, R.S.; Kite, S.V.; Garadkar, K.M. Bio-mediated synthesis of ZnO nanostructures for efficient photodegradation of methyl orange and methylene blue. *J. Mater. Sci. Mater. Electron.* **2021**, *32*, 28573–28586. [CrossRef]

56. Shahzad, R.; Muneer, M.; Khalid, R.; Amin, H.M.A. ZnO-Bi_2O_3 Heterostructured Composite for the Photocatalytic Degradation of Orange 16 Reactive Dye: Synergistic Effect of UV Irradiation and Hydrogen Peroxide. *Catalysts* **2023**, *13*, 1328. [CrossRef]

57. Reynes, M.; Bouabidi, H.; Piombo, G.; Risterucci, A.M. Caracterisation des principales varietes de dattes cultivees dans la region du Djerid en Tunisie. *Fruits* **1994**, *49*, 289–298.
58. Afnor, Ø. *Recueil de Normes Françaises des Produits Dérivés des Fruits et Légumes jus de Fruits*; AFNOR: Paris, France, 1982; Volume 325.
59. Linden, G.; Lavoisier, É. *Techniques D'analyse et de Contrôle dans les Industries Agro-Alimentaires: Principes des Techniques D'analyse*; Tec & Doc: Paris, France, 1984.
60. Miller, G.L. Use of Dinitrosalicylic Acid Reagent for Determination of Reducing Sugar. *Anal. Chem.* **1959**, *31*, 426–428. [CrossRef]
61. Ben Thabet, I.; Besbes, S.; Masmoudi, M.; Attia, H.; Deroanne, C.; Blecker, C. Compositional, Physical, Antioxidant and Sensory Characteristics of Novel Syrup from Date Palm (*Phoenix dactylifera* L.). *Food Sci. Technol. Int.* **2009**, *15*, 583–590. [CrossRef]
62. AOAC. *Official Methods of Analysis*, 16th ed.; Association of Official Analytical Chemists: Washington, DC, USA, 1995.
63. Juntachote, T.; Berghofer, E.; Siebenhandl, S.; Bauer, F. Antioxidative effect of added dried Holy basil and its ethanolic extracts on susceptibility of cooked ground pork to lipid oxidation. *Food Chem.* **2007**, *100*, 129–135. [CrossRef]
64. Gursoy, N.; Sarikurkcu, C.; Cengiz, M.; Solak, M.H. Antioxidant activities, metal contents, total phenolics and flavonoids of seven Morchella species. *Food Chem. Toxicol.* **2009**, *47*, 2381–2388. [CrossRef]